MIXING OF FLUIDS AND SOLIDS

Julio M. Ottino
Department of Chemical Engineering
Northwestern University
Evanston, Illinois 60208-3120
Phone: 847-491-3558
FAX: 847-491-3728
e-mail: ottino@chem-eng.nwu.edu

ABSTRACT

The work reported here focuses on mixing of fluids and mixing of solids; both areas involving theory and experiments. Within mixing of fluids we consider viscous mixing in 3D flows and mixing and dispersion of immiscible fluids. In the mixing of solids area we consider simultaneous mixing and segregation of powders in tumbling systems; the tools in this area being particle dynamics and Monte Carlo simulations, continuum and geometrical descriptions. The fluid aspects are reaching maturity; the solids area is newer and significant inroads have been made in the last two years especially in problems involving competition between mixing and segregation; the bulk of the attention is given to this area.

INTRODUCTION

Mixing is so widespread in technology and nature that one might expect that a comprehensive theory would have been developed ln be gained by a unified approach and by contrasting extremes, in this case mixing of fluids and mixing of dry powders. This idea is not new. The first views -- and vocabulary -- of solid mixing were based on analogies with mixing of fluids.[0] Recent developments provide clues for cross-fertilization. For example, under certain circumstances, both problems -- mixing of fluids and mixing of powders -- can be described by maps. And, as we demonstrate, chaos concepts which proved useful in the analysis of mixing of fluids, apply also to solid mixing.

MIXING OF FLUIDS

A complete description of the mixing of fluids is far from trivial and may well never be attained. The underlying physical processes are however clear. Exceptions notwithstanding, the Navier-Stokes equations govern flow; diffusional processes, if present, are well described by Fick's law; interfacial conditions by the Young-Laplace equation, and so on. The stumbling block was that, until recently, it was unclear how to apply the considerable mathematical apparatus of fluid mechanics to mixing.

The 2D picture is now clear: Dye structures in time-periodic flows evolve in an iterative fashion: an entire structure is mapped into a new structure with persistent large-scale features and with finer and finer scale features revealed at each period of the flow. The 3D picture is considerably less clear. Another issue is that the bulk of mixing work to date has been for the case of single-phase fluids. Much remains to be done for the case of two-phase systems.

MIXING OF SOLIDS

It may naively be argued that, as in the case of the mixing of fluids, the underlying physical processes governing granular mixing are clear as well -- one knows how particles interact: normal forces are Hertzian, tangential forces are Coulombic, etc. This is misleading. Little is known about cooperative phenomena and it is at this length scale that granular materials part company with their fluid counterparts; averaging, the cornerstone of continuum field descriptions, may not work. But probably the most crucial difference is *segregation*:. In granular materials mixing and segregation come together. In solids, more "agitation" does not imply better mixing. Granular mixtures of dissimilar (and not-too-dissimilar) materials often segregate when shaken or tumbled. Thus, for example, differences in *size* result in *percolation* of smaller particles in flowing layers[1], differences in *size* [2] or *density* [3] result in *radial* and *axial* segregation.

PROGRAM'S PHILOSOPHY: WHY FOCUS ON MIXING?

Why focus on mixing? Unarguably the first part of the answer has to do with the practical implications of the results. A second aspect is somewhat less obvious, and applies to both fluids and solids. Consider the case of solids, which is probably somewhat more dramatic. Solutions of *flow* problems for granular materials are rare, and there are only few instances of direct comparison of theoretical predictions to experimental results. Mixing experiments, in contrast, generate over long times *large scale patterns and structures which can be easily visualized.* (see for example [4]). Thus mixing studies provide a means of studying mechanisms of flows which are otherwise difficult to probe experimentally. There is another aspect as well: a failure to capture large scale phenomena serves as a litmus test of theories and computational models.

FLUID MIXING AND SOLID MIXING ANALOGIES

As discussed earlier, under certain circumstances both mixing of fluids and mixing of solids can be described by maps. This is true for example when mixing of solids proceeds by avalanches. This idea leads to several applications.[5] Other analogies can be readily exploited as well. Fluid mixing theory says that steady 2D flows are poor mixers. Thus one may easily deduce that *powder* mixing occurs more "slowly" in the continuous steady flow regime than in the discrete, time-periodic, avalanching case: it takes more *rotations* to achieve the same mixing in the continuous flow regime. The question is then how to make the continuous flow chaotic. Another example is the case of 3D cylinders. Axial mixing, essentially diffusive, is very slow. Chaos concepts are useful again: Faster overall mixing can be achieved by a combination of avalanches: rotation and "wobbling" of the axis of the cylinder.

Mixing in 3D Flows

A topic of current interest is complex 3D flows; this is an area were there is an imbalance towards computations.[6] Figure 1 shows some of our preliminary results in a system that we call the "fundamental mixing tank". Our philosophy here is that rather than going towards realism and try to simulate an actual stirred tank we conduct controlled experiments and high precision computations in a system that contains the essential elements of a full tank, as shown in Figure 1. All indications are that we have a good match between experiment and computations and we expect that this system will become a paradigm for and inspire advances on theoretical descriptions of mixing.

Mixing of Immiscible Fluids and Dispersion

Mixing and dispersion of viscous fluids -- blending in the polymer processing literature -- is the result of complex interaction between flow and events occurring at drop length-scales: breakup, coalescence and hydrodynamic interactions. Similarly, mixing and dispersion of powdered solids in viscous liquids is the result of complex interaction between flow and events -- erosion, fragmentation and aggregation -- occurring at agglomerate length scales. Important applications of these processes include the compounding of molten polymers, and the dispersion of fine particles in polymer melts. The following analogies are apparent:

breakup ↔ *fragmentation*

coalescence ↔ *aggregation*

The ratio of deforming viscous forces to resisting interfacial tension forces in the case of droplets is the *capillary number*, Ca. Similarly, the ratio of viscous to cohesive forces in agglomerates is the *fragmentation number*, Fa. Thus $\mathrm{Ca}<O(1)$ and $\mathrm{Fa}<O(1)$ determine conditions where no breakup or fragmentation is possible. Both processes, breakup and coalescence, for drops, and fragmentation and aggregation, for solids, lead to time-varying distributions of drops and cluster sizes which become time-invariant when scaled in suitable ways. Two areas have been pursued -- breakup and coalescence of immiscible fluids, and aggregation and fragmentation of solids in viscous liquids. The primary objective of our work in this area is to pursue both topics in parallel highlighting connections as to increase understanding. *Self-similarity* is common to all these problems; examples arise in the context of the distribution of stretchings within chaotic flows, in the asymptotic evolution of fragmentation processes, and in the equilibrium distribution of drop sizes generated upon mixing of immiscible fluids. A comprehensive summary of our results appears in [7] and [8].

Mixing and Segregation of Solids

Studies in this area involve the confluence of several tools: Monte Carlo simulations, this being restricted to flowing layers, particle dynamics, and constitutive based continuum descriptions.

Particle Dynamics

Particle dynamics methods (PD) [9,10] are eminently suited to study mixing and segregation -- particle properties can be varied on a particle-by-particle basis, allowing close matching between computations and experiments. In addition detailed mixed structures are easily captured and visualized. This method, however, is computationally intensive. These techniques have been used in two different ways:

- Studies of segregation in flowing layers. These studies are used to investigate constitutive models for segregation fluxes.
- Studies of mixing systems in terms of "hybrid" techniques.

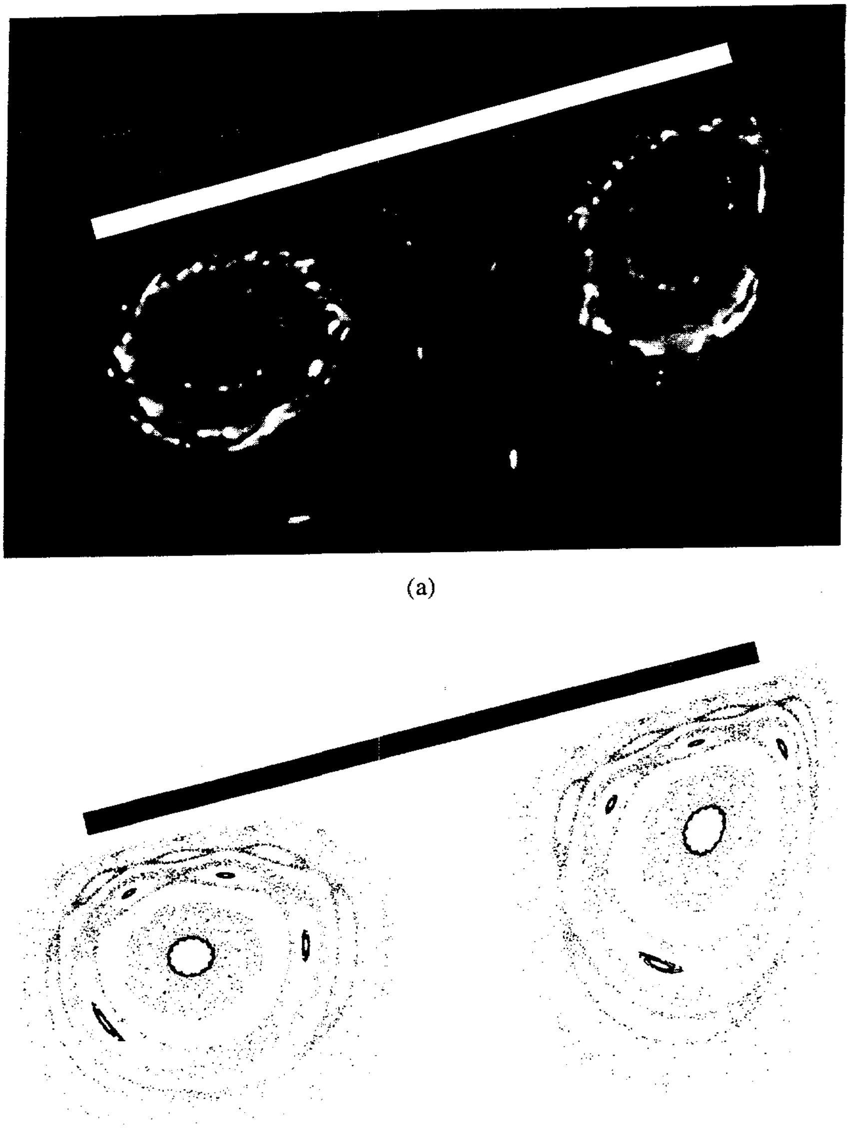

(a)

(b)

Figure 1 – Area below the impeller for the fundamental mixing tank. Impeller angle=14.3°, Re=7.0. (a) Experimental cross sectional photo of the flow illuminated with a sheet of laser light (white band is impeller location), and (b) the numerical Poincaré section.

Monte Carlo Simulations

An alternative to PD methods -- and a much less time (or CPU) consuming way -- of studying segregation is by means of Monte Carlo techniques.[11,12,13,14,15] While the results of Monte Carlo simulations only approximately describe the actual physical system (particles are assumed to be perfectly elastic), they yield good agreement with PD simulations when used to investigate constitutive descriptions of segregation fluxes in flowing layers.

Hybrid Simulations

In many cases of practical interest -- such as in a tumbler mixer, where the bulk of the particle motion consists of a solid body rotation -- it is not necessary to explicitly calculate the motion of all of the particles. By combining particle dynamics and geometrical insight -- in essence, by *focusing* the particle dynamics simulation only where it is needed -- a new hybrid method of simulation, which is much faster than a conventional particle dynamics method, has been devised. This technique can yield, according to flow conditions, up to more than an order of magnitude increase in computational speed. This allows simulations of the order of 10^4 particles on a typical workstation (see Figure 2[16]). Segregation problems in mixers with realistic diameter to particle size ratios can thus be studied.

Phenomenological Model of Segregation

We have proposed and tested the idea that, in the case of a mixture of particles with different densities, the driving force for segregation can be described in terms of an effective "buoyant force." The idea can be applied to a flowing layer and tested by means of computer simulations (PD and MC), and subsequently incorporated into models of competing mixing and segregation in rotating tumblers.[17] Denote by J_{sy} the segregation flux of the more dense particles and by ϕ_1 the volume of the denser particles. The segregation flux is

$$J_{sy} = -C\phi_1(\rho_1 - \langle\rho\rangle)g\cos\theta \tag{1}$$

where the average density is given by

$$\langle\rho\rangle = \frac{\rho_1\phi_1 + \rho_2\phi_2}{\phi_1 + \phi_2} \tag{2}$$

balance equation for steady flow down an inclined plane resulting from a balance between segregation and diffusion in the layer at equilibrium isand C is an unknown function which is a measure of the resistance to local motion. The species

$$\frac{d}{dz}\left(-D\phi_t\frac{df}{dz} + J_{sy}\right) = 0 \tag{3}$$

where z is he direction normal to the flow, $f=\phi_1/\phi_t$, is the volume fraction of the more dense particles, $\phi_\tau = (\phi_1 + \phi_2)$is the total solids volume fraction, D is the diffusivity and J_{sy} is the segregation flux of the more dense particles. Substituting the heuristic buoyancy flow into equation (3) and integrating yields the equilibrium volume fraction profile

$$\ln\left(\frac{f}{1-f}\right) = -\frac{K_s R}{D}(1-\overline{\rho})\overline{z} + \ln\left(\frac{f_o}{1-f_o}\right) \tag{4}$$

where K_S is the characteristic segregation velocity (a key assumption made while obtaining the above equation is that the ratio (K_s/D) is constant across the layer). Thus a plot of ln(f/1-f) versus distance should produce a straight line. Both PD and MC simulations verify this prediction.

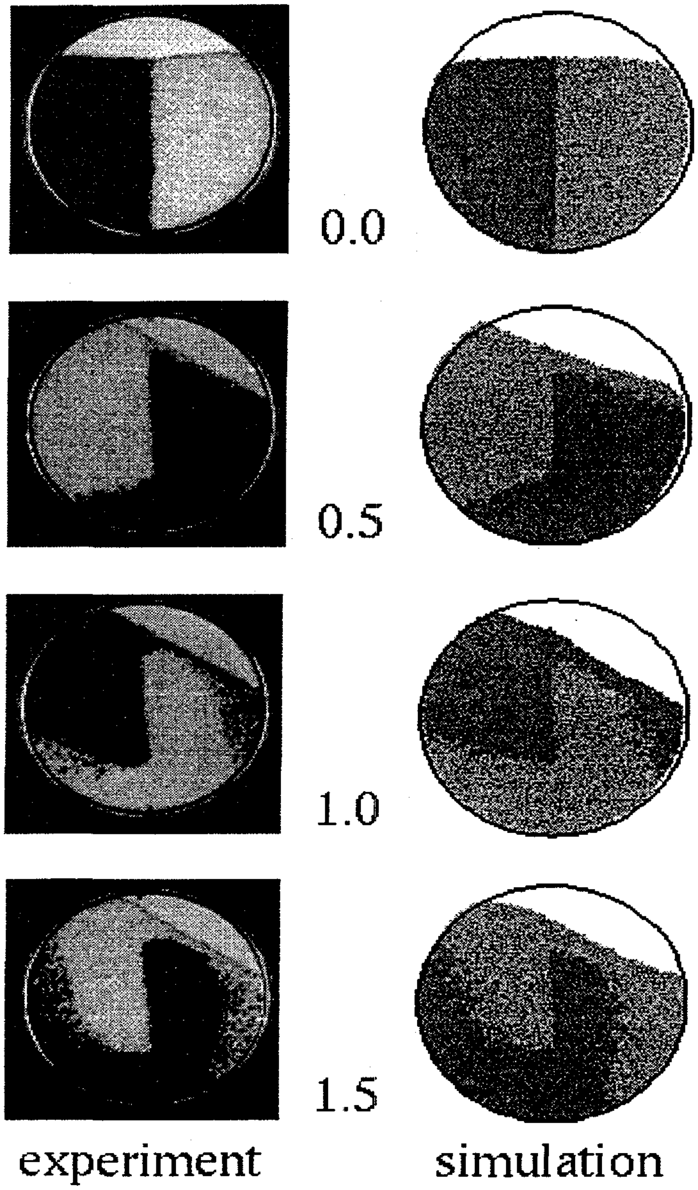

Figure 2 : Hybrid Comparison of Mixing for Avalanching. A comparison of mixing in the avalanching regime for an experiment (left) and simulation (right) at different times. From top to bottom are: the initial condition, after one half revolution, after one revolution, and after one and one half revolution.

In principle the constitutive model can then be incorporated into a general description of mixing and segregation,

$$\frac{\partial\phi_1}{\partial t}+v_x\frac{\partial\phi_1}{\partial x}+v_y\frac{\partial\phi_1}{\partial y}=\frac{\partial}{\partial x}\left(D\phi_t\frac{\partial f}{\partial x}-J_{sx}\right)+\frac{\partial}{\partial y}\left(D\phi_t\frac{\partial f}{\partial y}-J_{sy}\right) \tag{5}$$

where **J** = (J_{sx}, J_{sy}) is the segregation flux of the more dense particles; actual simulations though are conducted by means of a Lagrangian approach. Consider one example of the application of the theory and the ability to reproduce experimental results. The objective is to homogenize an initially segregated mixture. Figure 3 shows an example of such a process, in which an initially segregated state evolves to an equilibrium distribution. Time evolution computations show that the model captures interesting trends: often the system is better mixed at intermediate times; after partial mixing the system unmixes.[18]

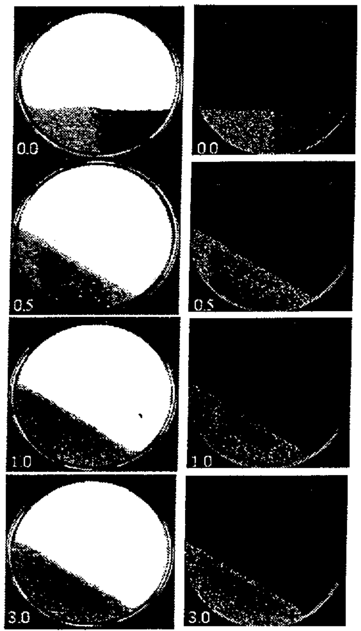

a) experiment simulation

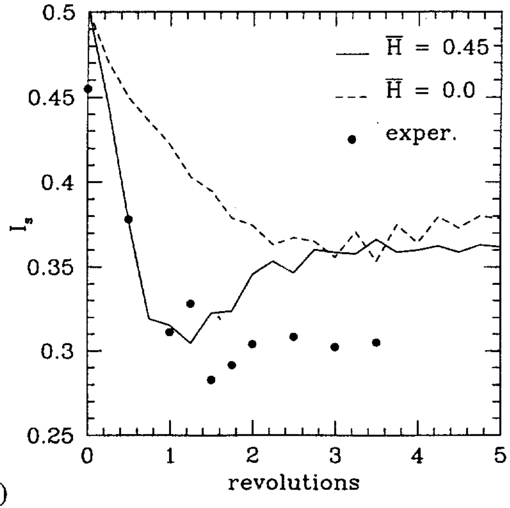

b)

Figure 3: (a)Time evolution of the distribution of a mixture of particles of different density with rotation of the cylinder obtained experimentally (left) and from theory (right). Rotational speed of the cylinder is 3 r.p.m. Darker particles in the simulations have higher density. (b) Variation of the intensity of segregation with cylinder revolutions for the pictures in (a) obtained from experiments and Lagrangian simulations.

Chaotic advection, which has been central in advancing the understanding of the fundamentals of liquid mixing[3], is also present in granular flows. We demonstrated this idea for the case of mixing of similar cohesionless powders, when segregation effects are unimportant. When the cross-section of the rotating container is circular, the mean flow is time-independent, and the streamlines (lines tangent to mean velocity field) act as impenetrable barriers to convective mixing. Is there any way to speed up the mixing by increasing the contribution of convection? Several studies of fluid flows show that time modulation of streamlines -- such that there are intersections between streamlines obtained at different times -- is generally sufficient to produce chaotic advection.[3] *In a rotating tumbler this simply happens when the cross-section is not circular.* We have demonstrated this idea in terms of computations in circular (as a reference case) and elliptical containers and experiments and computations in square containers (Figure 4).

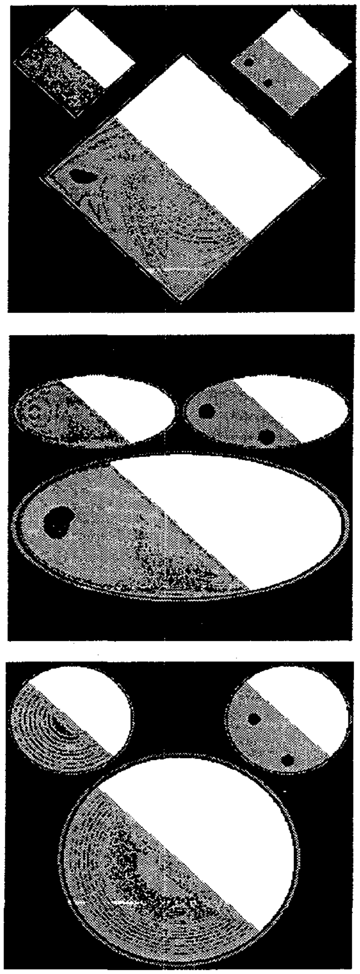

Figure 4: Comparison of the mixing of tracer particles in a circular, elliptical, and square mixer simulated using the model with no particle diffusion. The inset figure on the upper left shows the Poincaré section, and the initial condition is shown in the upper right inset. The cross-sectional areas of the mixers are equal so that the amount of material mixed in each case is identical, as is the rotational speed so that the mixing times are the same.

ACKNOWLEDGMENT

This work has been supported by U.S. Department of Energy, Office of Basic Energy Sciences, under grant DE-FG02-95ER14534, monitored by Dr. Robert Price.

REFERENCES

[0] Lacey, P.M., Developments in the theory of particle mixing, *J. Appl. Chem.*, **4**, 257-268 (1954).

[1] Savage, S. B. and Lun, C. K. K., Particle size segregation in inclined chute flow of dry cohesionless granular materials, *J. Fluid Mech.*, **189**, 311-335 (1988).

[2] Donald, M. B. and Roseman, B., Mixing and demixing of solid particles. Part 1. Mechanisms in a horizontal drum mixer, *Brit. Chem.`Eng.*, **7**, 749-753 (1962).

[3] Ristow, G. H., Particle mass segregation in an two-dimensional rotating drum, *Europhys. Lett.*, **28**, 97-101 (1994).

[4] Metcalfe, G., Shinbrot, T., McCarthy, J. J., and Ottino, J. M., Avalanche mixing of granular solids, *Nature*, **374**, 39-41 (1995).

[5] McCarthy, J.J., Shinbrot, T., Metcalfe, G., and Ottino, J.M., Mixing of granular materials in slowly rotated containers, *AIChE J*, **42**, 3351-3363 (1996).

[6] Tanguy, P.A., Lacroix, R., Bertrand, F., Choplin, L., and Brito-de La Fuente, E., Finte element analysis of viscous mixing with an HRS impeller, *AIChE J*, 38, 939-944 (1992)

[7] J.M. Ottino, P. de Rousell, S. Hansen, and D.V. Khakhar, Mixing and Dispersion of Viscous Fluids and Powdered Solids, *Advances in Chemical Engineering,* to appear 1998;

[8] S. Hansen, D.V. Kkakahr, and J.M. Ottino, Dispersion of Solids in Nonhomogeneous Viscous Flows, *Chem. Eng. Sci.* to appear 1998.

[9] Campbell, C. S., and Brennen, C. E., Chute flows of granular material: some computer simulations. *J. Appl. Mech.* **52**, 172-178 (1985).

[10] Cundall, P. A., and Strack, O. D. L., A discrete numerical model for granular assemblies. *Geotechnique* **29**, 47-65 (1979).

[11] Moradi, M. and Rickayzen, The structure of a hard sphere fluid mixture confined to a slit, *Molecular Phys.*, **66**, 143-160 (1989).

[12] Tan, Z., Marini Bettolo Marconi, U., van Swol, F., and Gubbins, K. E., Hard-sphere mixtures near a hard wall, *J. Chem. Phys.*, **90**, 3704-3712 (1989).

[13] Denton, A. R. and Ashcroft, N. W., Weighted density functional theory of non-uniform fluid mixtures: Application to the structure of binary hard sphere mixtures near a hard wall, *Phys. Rev. A*, **44**, 8242-8248 (1991).

[14] Rosato, A., Prinz, F., Standburg, K. J., and Svendsen, R., Monte Carlo simulation of particulate matter segregation, *Powder Technol.*, **49**, 59-69 (1986); Why Brazil nuts are on top: size segregation of particulate matter by shaking, *Phys. Rev. Lett.*, **58**, 1038-1040 (1987).

[15] Julien, R., Meakin, P., and Pavlovitch, A., Three-dimensional model for particle-size segregation by shaking, *Phys. Rev. Lett.*, **69**, 640-643 (1992).

[16] J.J. McCarthty and J.M. Ottino, Particle Dynamics Simulation; A Hybrid technique Applied to Granular Mixing, *Powder Tech.* submited 1997.

[17] D.V. Khakhar, J.J. McCarthy, T. Shinbrot, and J.M. Ottino, Transverse Flow and Mixing of Granular Materials in A Rotating Cylinder, *Phys. Fluids*, **9**, 31-43 (1997).

[18] D.V. Khakhar, J.J. McCarthty, and J.M. Ottino, Radial Segregation of Granular Mixtures in Rotating Cylinders, *Phys. Fluids*, 9, 3600-3614 (1997)

TRANSPORT PROPERTIES OF POROUS MEDIA FROM THE MICROSTRUCTURE

S. Torquato

Department of Civil Engineering & Operations Research and Princeton Materials Institute
Princeton University, Princeton, N.J. 08544

ABSTRACT

The determination of the effective transport properties of a random porous medium remains a challenging area of research because the properties depend on the microstructure in a highly complex fashion. This paper reviews recent theoretical and experimental progress that we have made on various aspects of this problem. A unified approach is taken to characterize the microstructure and the seemingly disparate properties of the medium.

I. INTRODUCTION

The purpose of this paper is to review progress that we have made in the last three years on five basic aspects of the problem of determining effective transport properties of random porous media: (i) quantitative characterization of the microstructure of nontrivial models; (ii) 3D imaging of porous media using x-ray tomography; (iii) derivation of predictive formulas on transport properties in terms of statistical correlation functions; (iv) derivation of rigorous cross-property relations; (v) and reconstruction of porous media.

II. AVERAGED EQUATIONS

The random porous medium is a domain of space $\mathcal{V}(\omega) \in \boldsymbol{R}^3$ (where the realization $\boldsymbol{\Omega}$ is taken from some probability space ω) of volume V which is composed of two regions: the pore region $\mathcal{V}_1(\omega)$ (in which transport occurs) of volume fraction (porosity) ϕ_1 and a solid-phase region $\mathcal{V}_2(\omega)$ of volume fraction ϕ_2. Let $\partial\mathcal{V}$ be the surface between $\mathcal{V}_1$ and $\mathcal{V}_2$.

The *effective conductivity* σ_e is given by an averaged Ohm's law:

$$< \mathbf{J}(\mathbf{x}) >= \sigma_e < \mathbf{E}(\mathbf{x}) > \tag{1}$$

where $< \mathbf{E}(\mathbf{x}) >$ and $< \mathbf{J}(\mathbf{x}) >$ represent the *ensemble average* of the local electric and current density fields, respectively. The local fields satisfy the usual steady-state conduction equations [1,2]. By mathematical analogy, results for σ_e translate into equivalent results for the thermal conductivity, magnetic permeability, dielectric constant, and diffusion coefficient.

The *mean survival time* τ of a Brownian particle diffusing in the fluid phase of a porous medium with an absorbing pore-solid interface is related to the average magnetization density obtainable from a nuclear magnetic resonance (NMR) experiment [2,3]. τ depends on the average pore size and diffusion coefficient D.

The *fluid permeability* k of a porous medium, defined by Darcy's law,

$$< \mathbf{u}(\mathbf{x}) >= -\frac{k}{\mu}\nabla p_o(\mathbf{x}) \,, \tag{2}$$

governs the rate at which a viscous fluid flows through it [4]. Here $< \mathbf{u}(\mathbf{x}) >$ is the ensemble average of the local fluid velocity which satisfies the steady-state Stokes equations [5], $\nabla p_o(\mathbf{x})$ is the applied pressure gradient, and μ is the dynamic viscosity. k depends nontrivially on the pore geometry and may be regarded to be an *effective cross-sectional area of pore channels.*

The *effective elastic tensor* $\mathbf{C}_e$ is given by an averaged Hooke's law:

$$< \Sigma(\mathbf{x}) >= \mathbf{C}_e < \epsilon(\mathbf{x}) > \tag{3}$$

where $< \epsilon(\mathbf{x}) >$ and $< \Sigma(\mathbf{x}) >$ represent the *ensemble average* of the local strain and stress fields, respectively. The local fields satisfy the equilibrium equations [5]. The attenuation of elastic waves in fluid-saturated porous media depends on their effective elastic moduli.

III. MICROSTRUCTURE CHARACTERIZATION

There are a variety of different types of statistical correlation functions that have arisen in rigorous expressions for transport properties. Until recently, application of such expressions (although in existence for almost thirty years in some cases) was virtually nonexistent because of the difficulty involved in ascertaining the correlation functions.

A. Unified Theoretical Approach

For statistically inhomogeneous systems of N identical d-dimensional spheres, Torquato [6] has introduced the general n-point distribution function $H_n(\mathbf{x}^m;\ \mathbf{x}^{p-m};\ \mathbf{r}^q)$ and found a series representation of H_n which enables one to compute it. From the general quantity H_n one can obtain all of the correlation functions that arise in rigorous property relations and their generalizations. This formalism has been generalized to treat polydispersed spheres, anisotropic media (e.g., aligned ellipsoids and cylinders), and cell models.

The preponderance of previous studies have focused on statistically homogeneous media. Significantly less research has been devoted to the study of *statistically inhomogeneous (non-ergodic)* two-phase media and yet porous media frequently has this feature [5]. We have proposed such a model consisting of inhomogeneous fully penetrable (Poisson distributed) spheres [7]. This model can be constructed for any specified variation of volume fraction (see Fig. 1) and permits one to evaluate the general n-point distribution function H_n. *Unlike the case of statistically homogeneous media, the microstructure functions depend upon the absolute positions of their arguments.*

We have also studied the lineal path function [8] and cluster statistics [9,10] for the prototypical continuum percolation model of d-dimensional overlapping spheres. For $d = 3$, we have computed the percolation threshold and critical exponents with heretofore unattained accuracy [11]. For the non-equilibrium random sequential addition process, we found exact expressions for the nearest-neighbor functions for lamellar media [12]. The full distribution of local volume fraction fluctuations in models of random media have been evaluated [13].

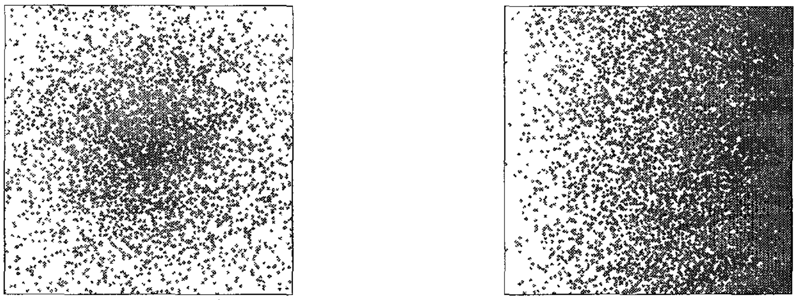

(a) (b)

Figure 1: Examples of statistically inhomogeneous particles: system (a) is under an "anti-centrifugal" field and system (b) has a linear grade in the volume fraction.

We have studied fundamental questions pertaining to the structure of dense hard-sphere systems along the metastable amorphous branch via molecular dynamics simulations [14,15]. For example, contrary to many previous studies, we found no existence of thermodynamic glass transition and found that the metastable system eventually crystallizes.

IV. 3D IMAGING VIA TOMOGRAPHY

We have very recently obtained a high-resolution $3D$ digitized representation of a Fountainebleu sandstone (see Fig. 2) using synchrotron-based X-ray tomographic techniques [16]. This digitized representation was used to extract a number of morphological characteristics of the sample, including the pore-size functions (see Fig. 3), enabling us to predict the transport properties of the rock. We have also employed the same technique to study the microstructure and properties of a porous gel [17].

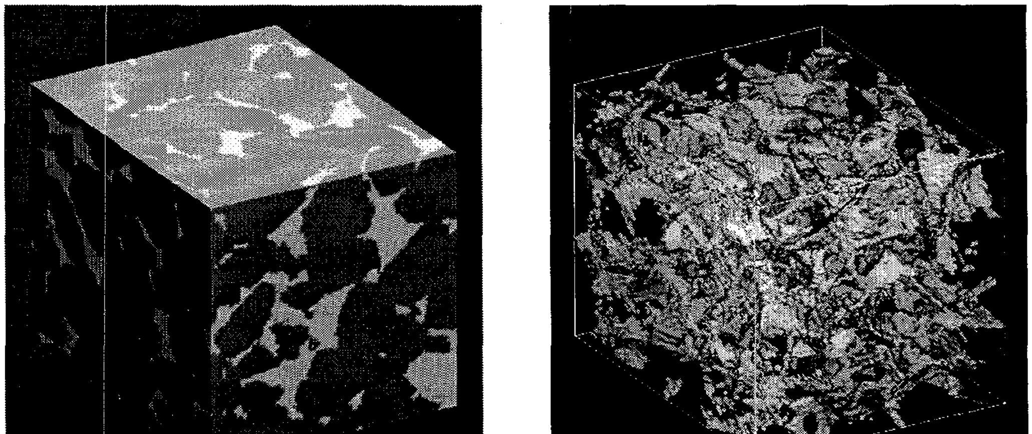

Figure 2: Surface cut (left) and pore space (right) of a $128 \times 128 \times 128$ pixels sub-region of the Fontainebleau sandstone.

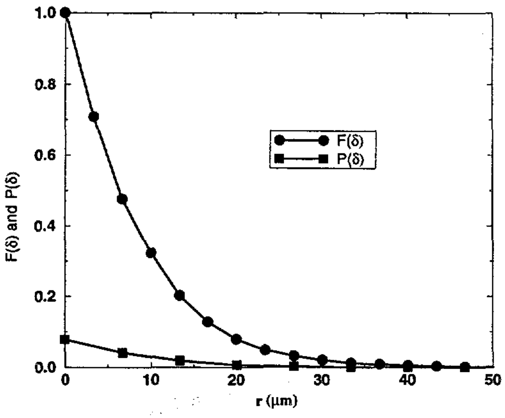

Figure 3: Pore-size distribution function $P(\delta)$ and the cumulative pore-size distribution function $F(\delta)$ for Fontainebleau sandstone.

V. MICROSTRUCTURE/PROPERTY CONNECTION

A. Rigorous Bounds

We have derived and computed bounds on the effective conductivity and elastic moduli of realistic models of random media which depend upon the microstructure through various sets of correlation functions and symmetry information [18-20]. We developed rigorous bounds on the effective conductivity σ_e of dispersions that are given in terms of the phase contrast between the inclusions and matrix, the *interface properties*, volume fraction, and higher-order morphological information [21].

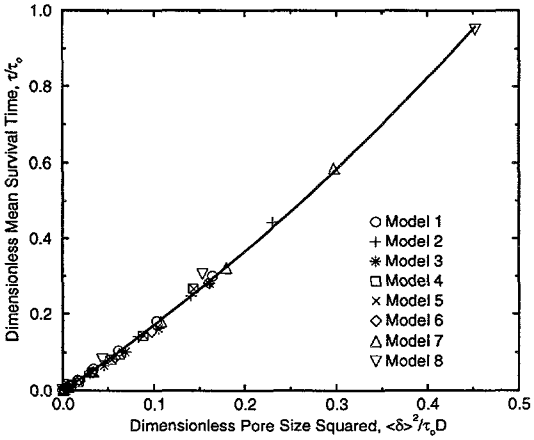

Figure 4: Dimensionless mean survival time τ/τ_o versus dimensionless mean pore size squared $\langle\delta\rangle^2/\tau_o D$ for all models 1–8. Solid curve is universal scaling relation.

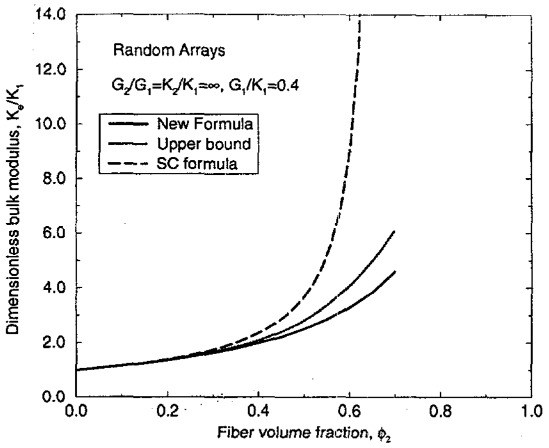

Figure 5: Dimensionless effective transverse bulk modulus K_e/K_1 vs. fiber volume fraction ϕ_2 for random arrays of circular superrigid fibers in a compressible matrix. Note that the self-consistent (SC) formula violates the upper bound.

Guided by rigorous bounds on the mean survival time τ, we have found a universal scaling [22] for τ (see Fig. 4) which is well represented by the simple expression

$$\frac{\tau}{\tau_o} = \frac{8}{5}x + \frac{8}{7}x^2, \tag{4}$$

where $x = \langle\delta\rangle^2/\tau_o D$ is the dimensionless mean pore size squared.

B. Exact Results

For the special case of periodic arrays, we have obtained exact results for the effective conductivity for both the interfacial resistance case [23] and interfacial conductance case [24].

We have derived new, exact series expansions for the effective elastic tensor of anisotropic, d-dimensional, two-phase disordered composites whose nth-order tensor coefficients are integrals involving n-point correlation functions that characterize the structure [25,26]. These series expansions, valid for any structure, perturb about certain optimal dispersions. Third-order truncation of the expansions results in formulas for the elastic moduli of isotropic dispersions that are in very good agreement with benchmark data, always lie within rigorous bounds, and are superior to popular self-consistent approximations (Fig. 5).

C. Field Fluctuations

When a composite is subjected to a constant applied electric, thermal or stress fields, the associated local fields exhibit strong spatial fluctuations. We have calculated the local electric field (i.e., all moments of the field) for various random-media models by solving the governing partial differential equations using efficient and accurate integral equation techniques [27]. In general, the probability density function associated with the electric field exhibits a double-peak character and therefore is highly non-Gaussian.

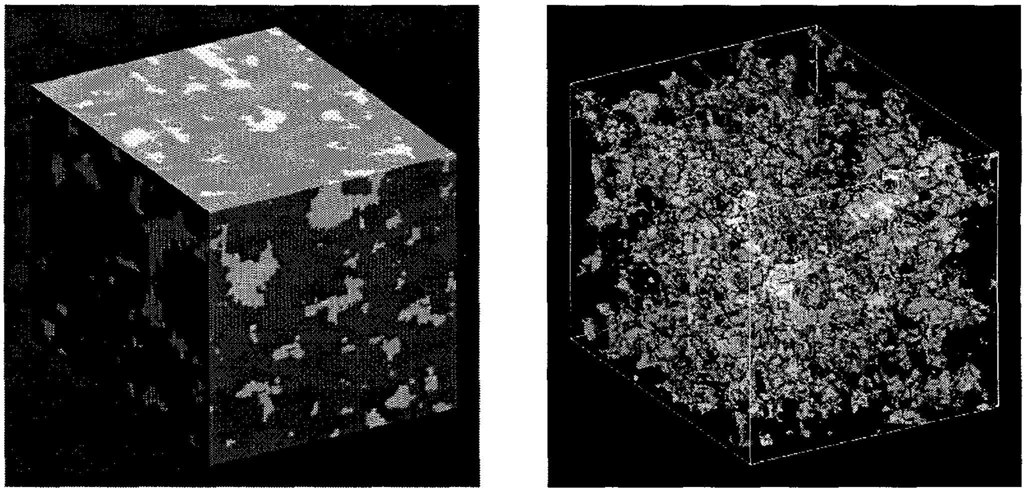

Figure 6: Reconstruction of Fontainebleau sandstone (Fig. 2) using two-point correlation function and lineal path function. Surface cut (left) and pore space (right).

VI. CROSS-PROPERTY RELATIONS

An intriguing fundamental as well as practical question in the study of heterogeneous materials is the following: Can different properties of the medium be *rigorously* linked to one another? Such cross-property relations become especially useful if one property is more easily measured than another property; e.g., it is difficult to measure the permeability k in situ.

We have continued to seek and test cross-property relations that connect the fluid permeability of porous media with diffusion properties, such as diffusion relaxation times, obtainable from NMR experiments, and the *electrical conductivity* or its inverse denoted by F. Rigorous results suggest that the approximate relation [28]

$$k \approx \phi_1 \frac{D\tau}{F} \, . \tag{5}$$

should be accurate for a large class of porous media.

To test cross-property relation (9), we have recently analyzed the 3D tomographic image of the aforementioned Fountainbleu sandstone (see Fig. 2) [16]. The quantity τD was determined to be 154 μm^2 from Brownian-motion simulations, $F^{-1} \approx 0.089$, and ϕ_1 was found to be 0.15. Thus, relation (9) predicts $k \approx 2.1 \mu m^2$, which is in relatively good agreement with the experimental value of 1.3 μm^2.

We have established rigorous cross-property bounds between the effective conductivity σ_e on the one hand and the effective bulk modulus K_e or shear modulus G_e on the other, for both two- and three-dimensional composites [29,30. These results have been recently extended to cracked media [31].

VII. RECONSTRUCTING POROUS MEDIA

We have formulated a procedure to reconstruct general digitized random heterogeneous materials (e.g., composites) that is simple to implement and can incorporate any type and number of correlation functions in order to provide necessary information for accurate reconstruction [32]. This procedure, based on *simulated annealing*, is an extension of our earlier work on particle systems [33]. We have examined reconstructions of known models of random media, constructions of heretofore unknown structures based on hypothetical correlation functions, and the reconstruction of a 3D sandstone structure using information obtained from a 2D micrograph or image [34] (see Fig. 6). The procedure sheds light on the nature of the information contained in correlation functions and can aid in classifying random media. It is shown that the structure factor obtained from scattering is usually not sufficient to reconstruct the material accurately.

We have also compared the macroscopic properties of the reconstructions to those of the original materials. For example, the mean survival time τ and the fluid permeability k are within about 15% of the corresponding values for the original sandstone.

ACKNOWLEDGMENTS

Support for this work was provided by the DOE under Grant DE-FG05-92ER14275.

REFERENCES

1. M. Beran, *Statistical Continuum Theories* (Wiley, New York, 1968).
2. S. Torquato, "Random Heterogeneous Media: Microstructure and Improved Bounds on Effective Properties," *Appl. Mech. Rev.* **44**, 37 (1991).
3. A. H. Thompson et. al., "Deuterium Magnetic Resonance and Permeability in Porous Media," *J. Appl. Phys.* **65**, 3259 (1989).
4. A. E. Scheidegger, *The Physics of Flow through Porous Media* (University of Toronto Press, Toronto, 1974).
5. R. M. Christensen, *Mechanics of Composite Materials* (Wiley, New York, 1979).
6. S. Torquato, "Microstructure Characterization and Bulk Properties of Disordered Two-Phase Media," *J. Stat. Phys.* **45**, 843 (1986).
7. J. Quintanilla and S. Torquato, "Microstructure Functions for a Model of Statistically Inhomogeneous Random Media," *Phys. Rev. E*, **55**, 1558 (1997).
8. J. Quintanilla and S. Torquato, "Lineal Measures of Clustering in Overlapping Particle Systems,"*Phys. Rev. E*, **54**, 4027 (1996).
9. J. Quintanilla and S. Torquato, "Clustering Properties of *d*-Dimensional Overlapping Spheres," *Phys. Rev. E* **54**, 5331 (1996).
10. J. Quintanilla and S. Torquato, "Clustering in a Continuum Percolation Model," *Adv. Appl. Probability*, **29**, 327 (1997).
11. M. D. Rintoul and S. Torquato, "Critical Threshold and Exponents in a 3D Continuum Percolation Model," *J. Phys. A: Math. & Gen.*, **30**, L585 (1997).
12. M. D. Rintoul, S. Torquato and G. Tarjus, "Nearest-Neighbor Statistics in a One-Dimensional Random Sequential Adsorption Process," *Phys. Rev. E*, **53**, 450 (1995).
13. J. Quintanilla and S. Torquato, "Local Volume Fractions Fluctuations" *J. Chem. Phys.* **106**, 2741 (1997).

14. M. D. Rintoul and S. Torquato, "Metastability and Crystallization in Hard-Sphere Systems," *Phys. Rev. Lett.*, **77**, 4198 (1996).
15. M. D. Rintoul and S. Torquato, "Computer Simulations of Dense Hard-Sphere Systems," *J. Chem. Phys.*, **105**, 9258 (1996).
16. D. Coker, S. Torquato, and J. Dunsmuir "Morphological and Physical Properties of Fountainebleu Sandstone from Tomography," *J. Geophys. Res.* **100**, 17497 (1996).
17. M. D. Rintoul, S. Torquato, C. Yeong, S. Erramilli, D. Keane, D. Dabbs, and I. A. Aksay, "Structure and Transport Properties of a Porous Magnetic Gel via X-ray Tomography," *Phys. Rev. E*, **54**, 2663 (1996).
18. J. Quintanilla and S. Torquato, "Microstructure and Conductivity of Hierarchical Laminate Composites," *Phys. Rev. E*, **53**, 4368 (1996).
19. L. V. Gibiansky and S. Torquato, "Geometrical Parameter Bounds on Effective Properties of Composites," *J. Mech. Phys. Solids*, **43**, 1587 (1995).
20. L. V. Gibiansky and S. Torquato, "Phase-Interchange Relations for the Elastic Moduli of Two-Phase Composites," *Int. J. Eng. Sci.*, **34**, 739 (1996).
21. S. Torquato and M. D. Rintoul, "Effect of the Interface on the Properties of Composite Media," *Phys. Rev. Lett.*, **75**, 4067 (1995).
22. S. Torquato and C. L. Y. Yeong, "Universal Scaling for Diffusion-Controlled Reactions Among Traps," *J. Chem. Phys.*, **106**, 8814 (1997).
23. H. Cheng and S. Torquato, "Effective Conductivity of Periodic Arrays of Spheres with Interfacial Resistance, *Proc. R. Soc. Lond. A*, **453**, 145 (1997).
24. H. Cheng and S. Torquato, "Effective Conductivity of Suspensions with a Superconducting Interface," *Proc. R. Soc. Lond. A* , **453**, 1331 (1997).
25. S. Torquato, "Exact Expression for the Effective Elastic Tensor of Disordered Composites," *Phys. Rev. Lett.* **79**, 681 (1997).
26. S. Torquato, "Effective Stiffness Tensor of Composite Media: I. Exact Series Expansions," *Journal of the Mechanics and Physics of Solids*, **45**, 1421 (1997).
27. H. Cheng and S. Torquato, "Electric Field Fluctuations in Random Dielectric Composites," *Phys. Rev. B*, **56**, 8060 (1997).
28. L. M. Schwartz, N. Martys, D. P. Bentz, E. J. Garboczi, and S. Torquato, "Cross-Property Relations in Model Porous Media," *Phys. Rev. E*, **48**, 4584 (1993).
29. L. V. Gibiansky and S. Torquato, "Rigorous Link Between the Conductivity and Elastic Moduli of Fiber-Reinforced Composite Materials," *Phil. Trans. R. Soc. Lond.*, **343**, 243 (1995).
30. L. V. Gibiansky and S. Torquato, "Connection Between the Conductivity and Elastic Moduli of Isotropic Composite Materials," *Proc. R. Soc. Lond. A*, **452**, 253 (1996).
31. L. V. Gibiansky and S. Torquato, "Bounds on the Effective Moduli of Cracked Materials," *J. Mech. Phys. Solids*, **44**, 233 (1996).
32. C. L. Y. Yeong and S. Torquato, "Reconstructing Random Media," *Phys. Rev. E*, **57**, 495 (1998).
33. M. D. Rintoul and S. Torquato, "Reconstruction of the Structure of Dispersions," *J. Colloid Interface Sci.*, **186** , 467 (1997).
34. C. L. Y. Yeong and S. Torquato, "Reconstructing Random Media: II. 3D Media from 2D Cuts," *Phys. Rev. E*, in press.

NUMERICAL SIMULATION OF MASS TRANSFER FOR BUBBLES IN WATER

Shom S. Ponoth and J.B. McLaughlin

Department of Chemical Engineering, Clarkson University
Potsdam, N.Y. 13699-5705

ABSTRACT

This paper presents numerical simulation results for the dissolution of isolated, steadily rising bubbles in water. The velocity field is computed on the assumption that the rate of dissolution is slow enough that the bubble size may be treated as quasisteady. Results are presented for bubbles having equivalent spherical diameters ranging from $0.7mm$ to $1.5mm$. The effects of sparingly soluble surfactants are included using the stagnant cap model. The results exhibit a very strong effect of the absorbed surfactant on the mass transfer rate.

INTRODUCTION

This paper will present numerical results for liquid phase mass transfer from bubbles in water. The bubbles of interest have equivalent spherical diameters between $0.7mm$ and $1.5mm$. In this regime, experiments indicate that the bubbles rise along rectilinear paths so that one can assume axisymmetric motion. The Reynolds numbers, based on the equivalent bubble diameter and the rise velocity, range from 55 to 535.

The mass transfer problem to be considered is the dissolution of a CO_2 bubble in water. For the purpose of computing the flow field, the bubbles are treated as voids. It is assumed that the rate of dissolution is small enough that the bubble radius and the bubble rise velocity may be treated as constant. Both clean and contaminated bubbles are considered. The contamination is modeled as an immobilized surfactant cap. Existing asymptotic results based on boundary layer theory will be compared with the numerical results.

Lochiel and Calderbank [1] developed a boundary layer theory for mass transfer in the continuous phase around spheroidal bubbles and drops. They assumed that the Peclet and Schmidt numbers were much larger than unity. Their analysis extended previous contributions by Boussinesq [2], Frössling [3], Griffith [4], Bowman et al. [5], and Friedlander [6, 7] for spherical objects. They considered both objects with free interfaces and objects with interfaces that were immobilized by surface active materials. For large Reynolds numbers, they based their calculations on potential flow solutions.

Since mass transfer was assumed to have a negligible effect on the size and rise velocity of the bubble, the fluid mechanics problem was decoupled from the mass transfer problem. The adaptive grid finite difference technique developed by Ryskin and Leal [8, 9, 10] was used to obtain the flow field for the computation of the concentration field. This technique was developed for axisymmetric bubbles or drops. In water, this limits the applicability of the technique to bubbles with equivalent spherical diameters smaller than about $1.9mm$ in pure water (Duineveld [11]) and somewhat smaller values in contaminated water (Haberman and Morton [12, 13], Saffman [14], and Hartunian and Sears [15].

For the bubbles considered in the study, it is feasible to calculate the concentration field by directly solving the governing partial differential equation (PDE). This is accomplished by choosing a distribution of grid points that places sufficient grid points within the mass transfer boundary layer.

COMPUTATION OF LIQUID VELOCITY FIELD

The numerical techniques used to compute the flow field around a bubble were described by McLaughlin [16]. Therefore, only a brief overview of the methods will be given here.

In what follows, the equivalent spherical radius, r_e, the bubble rise velocity, U, the liquid density, ρ, the fluid kinematic viscosity, ν, the interfacial surface tension for a clean interface, γ_0 ,and the acceleration of gravity, g, will be used to make quantities dimensionless. The gas density is assumed to be negligible. The Reynolds number, Re, the Weber number, W, and the Morton number, M, may be used to characterize the bubble motion for clean interfaces:

$$Re = \frac{d_e U}{\nu} \tag{1}$$

$$W = \frac{\rho d_e U^2}{\gamma_0} \tag{2}$$

$$M = \frac{g\mu^4}{\rho\gamma_0^3}. \tag{3}$$

The drag coefficient, C_D, is given by

$$C_D = \frac{4}{3}\frac{d_e g}{U^2}. \tag{4}$$

The above quantities are related by

$$M = \frac{3}{4}C_D\frac{W^3}{Re^4}. \tag{5}$$

Following Ryskin and Leal [8], it is convenient to introduce an orthogonal, curvilinear coordinate system (ξ,η,ϕ) in which the variables ξ and η lie between 0 and 1. The surface of the bubble is given by $\xi = 1$. The point at infinity corresponds to $\xi = 0$. The positive x axis corresponds to $\eta = 0$ and the negative x axis corresponds to $\eta = 1$. The coordinate mapping is determined by the covariant Laplace equations as described by Ryskin and Leal.

The present study is limited to axisymmetric motion. Therefore, it is convenient to use the streamfunction-vorticity method. For steady motion, the governing equations are

$$L^2(\omega\sigma) - \frac{Re}{2}(\frac{\partial\psi}{\partial\xi}\frac{\partial\omega/\sigma}{\partial\eta} - \frac{\partial\psi}{\partial\eta}\frac{\partial\omega/\sigma}{\partial\xi}) = 0 \tag{6}$$

$$L^2\psi + \omega = 0, \tag{7}$$

where

$$L^2 = \frac{1}{h_\xi h_\eta}[\frac{\partial}{\partial\xi}(\frac{f}{\sigma}\frac{\partial}{\partial\xi}) + \frac{\partial}{\partial\eta}(\frac{1}{f\sigma}\frac{\partial}{\partial\eta})]. \tag{8}$$

In eqs (6-8), ω is the ϕ component of the vorticity, ψ is the streamfunction, h_ξ and h_η are metric functions, and f is the distortion function, which is defined by $f = h_\eta/h_\xi$.

The pressure at the interface may be obtained by integrating the Navier-Stokes equation along the bubble surface:

$$p = \frac{3}{4}C_D x - u_\eta^2 - \frac{4}{Re}\int_0^\eta \frac{f}{\sigma}\frac{\partial}{\partial\xi}(\sigma\omega)d\eta, \tag{9}$$

where the pressure has been chosen to vanish at $\eta = 0$. By demanding that, in steady-state, the net force on the bubble vanishes, one may express C_D in terms of p_{dyn}, where p_{dyn} is the sum of the second and third terms on the right hand side of eq (9).

Clean Interfaces

For a clean interface, the boundary conditions at the surface of the bubble are:

$$\psi = 0 \tag{10}$$

$$\omega - 2\kappa_\eta u_\eta = 0 \tag{11}$$

$$\tau_{\xi\xi} - \frac{4}{W}(\kappa_\eta + \kappa_\xi) = 0. \tag{12}$$

In eqs (10-12), κ_η and κ_ξ are the normal curvatures, u_η is the η component of the liquid velocity, and $\tau_{\xi\xi}$ is a component of the liquid stress tensor at the interface. The normal curvatures may be computed from expressions given by Ryskin and Leal [9]. Equation (11) is the condition that the tangential stress should vanish. This condition follows from the assumption that the viscosity of the gas is negligible compared to the viscosity of the liquid. Equation (12) is the normal stress balance.

Contaminated Interfaces

McLaughlin [16] discussed the conditions for which the surfactant surface concentration can be modeled as a stagnant cap. In this regime, the surface concentration, Γ, and the surface velocity, u_s, reduces to

$$\nabla_s \cdot (\Gamma \mathbf{u_s}) = 0. \tag{13}$$

The solution is

$$u_\eta = 0,\ \theta < \phi \tag{14}$$

$$\Gamma = 0,\ \theta > \phi, \tag{15}$$

where ϕ is the cap angle. The angles ϕ and θ are measured from the positive x-axis. Thus, the fluid mechanics problem is decoupled from the mass transfer problem in this case. One specifies ϕ and then solves the Navier-Stokes equation subject to free-slip boundary conditions for $\theta > \phi$ and no-slip boundary conditions for $\theta < \phi$.

To determine the surface tension, γ, one imposes the tangential stress balance:

$$\tau_{\xi\eta} = -\frac{4}{h_\eta W}\frac{\partial \gamma'}{\partial \eta}. \tag{16}$$

In eq. (16), $\gamma' = \gamma/\gamma_0$, where γ_0 is the surface tension of the clean interface. After computing the flow field, one can compute the components of the liquid stress tensor and use eq. (16) to compute the dimensionless surface tension.

Although it was not done in the work to be presented, it is feasible to compute the volume concentration of surfactant, C, and to relate value of C at large distances from the bubble, C_∞, to the surfactant cap angle. In this paper, some results will be presented for the average value of C near the surface of the bubble, C_s. Although C_s will, in general, differ from C_∞, the numerical results of Cuenot et al. [17] for aqueous solutions of decanoic acid indicate that the average value of C_s is within a factor of $O(1)$ of C_∞ for bubbles in the size range of interest in the present paper. Therefore, one can use the average value of C_s to obtain a rough estimate of C_∞. An approximation for the average value of C_s may be obtained from the rate of adsorption of surfactant onto the bubble (see McLaughlin [16] for a more detailed discussion):

$$r_{ad} = \beta C_s'(\Gamma_\infty - \Gamma) - \alpha\Gamma. \tag{17}$$

In eq.(17), α and β are the desorption and adsorption rate constants, Γ is the surface concentration of surfactant, and Γ_∞ is the value of Γ at close-packing.

In the stagnant cap model, one can determine the surface tension from the tangential stress balance. Using an appropriate equation of state, one can determine Γ from γ. For many surfactants, the Frumkin equation provides a useful equation of state:

$$\gamma_0 - \gamma = -RT\Gamma_\infty ln(1 - \frac{\Gamma}{\Gamma_\infty}). \tag{18}$$

Table 1 provides the relevant parameters for decanoic acid.

Table 1: Parameters for decanoic acid.

Γ_∞ $(mole/m^3)$	α (s^{-1})	β $(m^3/(mole \cdot s))$	CMC $(mole/m^3)$
$5 \cdot 10^{-6}$	3.57	40	24

McLaughlin [16] found that, even for completely immobilized interfaces, the values of γ are only a few percent smaller than γ_0. If there is a 2% difference, the value of Γ is only about 11% of Γ_∞. Thus, it should be reasonable to simplify eq. (17) as follows:

$$r_{ad} = \beta C_s' \Gamma_\infty - \alpha\Gamma. \tag{19}$$

In steady-state, there should be no net rate of transfer of surfactant between the interface and the liquid. Therefore, if one averages eq. (19) over the bubble interface, one obtains the following expression for the average value of C_s':

$$< C_s' > = \frac{\alpha < \Gamma >}{\beta \Gamma_\infty}. \tag{20}$$

Numerical Algorithm and Parameters

The covariant Laplace equations and the streamfunction-vorticity equations were put into a canonical form discussed by Ryskin and Leal [9] and solved with the constant step ADI method that they suggested. In this approach, one uses an artificial time step, Δt, and relaxation parameters for the vorticity boundary condition, β_ω, and the normal stress balance, β_h. The spatial discretization is second order accurate. Ryskin and Leal suggest two scalings for the ADI equations. They report that one of them is more stable at large Reynolds numbers and or Weber numbers. The latter scaling was used in all the computations to be reported.

Ryskin and Leal [8, 9, 10] used the following form for the distortion function:

$$f = \pi\xi(1 - 0.5sin(\pi\eta)) \tag{21}$$

The distortion function in eq. (21) produces a useful distribution of grid points to resolve the momentum boundary layer near the bubble surface. However, the mass transfer boundary layer is thinner by a factor roughly equal to $1/Pe^{1/2}$ for a clean interface. Since $Sc = 500$ for CO_2 in water, one would expect the mass transfer boundary layer to be an order of magnitude thinner than the momentum layer. Therefore, it is convenient to modify the distortion function to concentrate more grid points near the surface of the bubble. For the computations to be reported,

$$f = \pi\frac{1}{b}(e^{b\xi} - 1)(1 - 0.5sin(\pi\eta)). \tag{22}$$

The constant b was chosen to be 2 or 3 in the computations of the liquid velocity field and the concentration field for runs in which the concentration field was computed by finite difference methods. It was found that this choice permitted a significant reduction in the total number of grid points in the ξ direction.

To compute the Reynolds and Weber numbers, an iterative procedure can be based on the following equation:

$$\frac{W}{Re^2} = \frac{\rho\nu^2}{\gamma d_e}. \tag{23}$$

Once one specifies the physical properties of the liquid and the size of the bubble, the ratio W/Re^2 is fixed. Thus, one can perform a run for values of W and Re that satisfy eq. (23) and determine the value of the Morton number. If the Morton number differs significantly from the value for water, one can select a second Reynolds number and compute the corresponding Weber number from eq.(23). In practice, only a few iterations are needed to obtain converged results.

FORMULATION OF MASS TRANSFER PROBLEM

The volume concentration of CO_2, c', is assumed to vanish at infinite distance from the bubble, which is stationary in the frame of reference for which the computations are performed. The volume concentration at the surface of the bubble is denoted by c'_s. The concentration field is assumed to obey the following PDE:

$$\frac{\partial c}{\partial t} + \mathbf{v} \cdot \nabla c = \frac{2}{Pe}\nabla^2 c, \tag{24}$$

where the c is the dimensionless concentration, which is defined by $c = c'/c'_s$.

It is useful to rewrite eq. (24) in terms of the orthogonal curvilinear coordinate system (ξ, η, ϕ):

$$\frac{\partial c}{\partial t} + v_\xi \frac{1}{h_\xi}\frac{\partial c}{\partial \xi} + v_\eta \frac{1}{h_\eta}\frac{\partial c}{\partial \eta} = \frac{2}{Pe}\frac{1}{h_\xi h_\eta \sigma}[\frac{\partial}{\partial \xi}(f\sigma\frac{\partial c}{\partial \xi}) + \frac{\partial}{\partial \eta}(\frac{\sigma}{f}\frac{\partial c}{\partial \eta})]. \tag{25}$$

The finite difference solution of eq. (24) is similar to the solution of eqs. (6)-(7). McLaughlin [16] described the solution of the latter equations. The concentration field is computing by an ADI time-stepping method:

$$c_{n+1/2} = c_n - \mathbf{v} \cdot \nabla c_n \Delta t + \frac{1}{h_\xi h_\eta}\frac{\partial^2 c_{n+1/2}}{\partial^2 \xi} \tag{26}$$

$$c_{n+1} = cn + 1/2 + \frac{1}{h_\xi h_\eta}\frac{\partial^2 c_{n+1}}{\partial^2 \eta}. \tag{27}$$

The operators in eqs (26) and (27) were discretized with central difference approximations at the interior points of the $\xi - \eta$ plane. Three point one-sided differences were used at the boundaries.

The surface flux and Sherwood number can be computed from the concentration profile.

RESULTS

Figure 1 shows the streamlines near a bubble. The equivalent spherical diameter of the bubble is $1mm$. The surfactant cap angle is 90^o. The presence of a wake region beneath the bubble is evident. In the bubble's frame of reference, the liquid velocity in the wake is small in magnitude compared to the free stream velocity. Also, the liquid in the wake has a large residence time and one might expect much of it to be nearly saturated. For these reasons, as pointed out by Lochiel and Calderbank [1] one might expect the wake region to contribute relatively little to the overall mass transfer rate. Later, this idea will be documented.

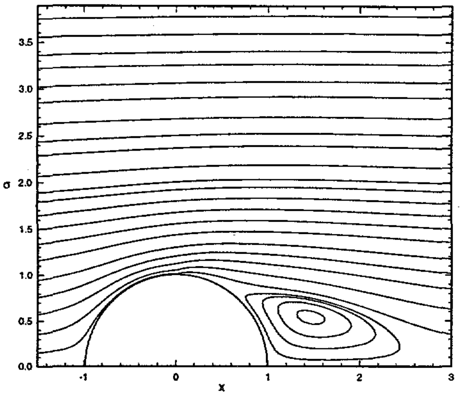

Figure 1: Streamlines around the bubble for $d_e = 1.0mm, \phi = 90°$.

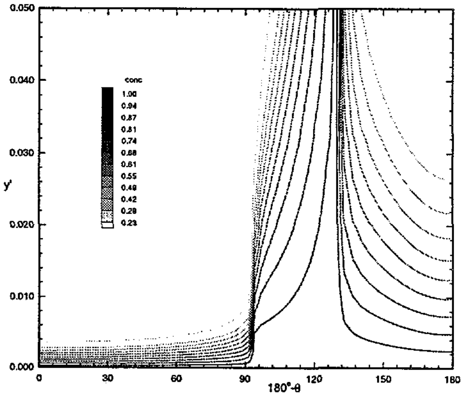

Figure 2: Concentration contours around the bubble for $d_e = 1.0mm, \phi = 90°$.

Figure 2 shows contours of the concentration field for the bubble in Fig. 1. The contours are shown in dimensionless boundary layer coordinates (x',y'), where x' is measured from the top of the bubble and y' is measured perpendicular to the bubble surface. At the leading edge of the surfactant cap, the concentration contours are pushed away from the bubble surface. This phenomenon is caused by the retardation of the tangential motion of the liquid by the surfactant cap that causes liquid to be pushed away from the bubble.

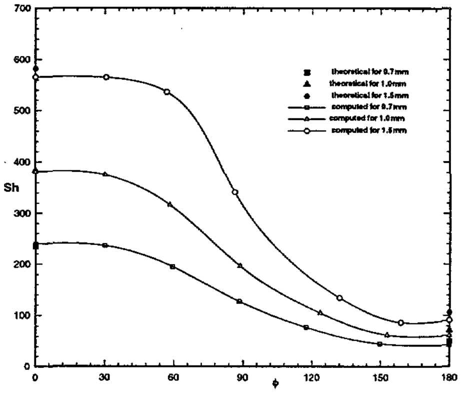

Figure 3: Comparison of computed and theoretical Sherwood numbers.

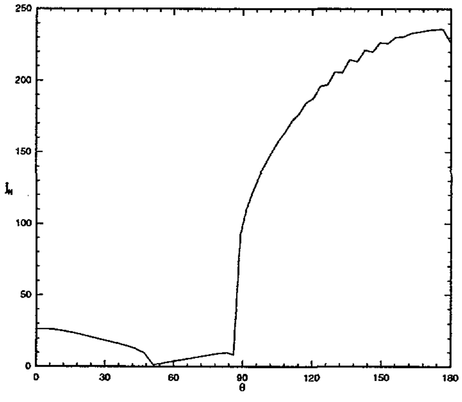

Figure 4: Surface flux.

Figure 3 shows the Sherwood number as a function of the cap angle for the three bubble sizes considered in this paper. It may be seen that the Sherwood number decreases almost monotonically with cap angle. The only deviations from monotonicity are probably due to numerical error. Some of the decrease is due to the immobilization of the interface and some of it is due to the formation of wake.

Figure 4 show the surface flux as a function of the polar angle for the bubble in Fig. 1. The flux is significantly smaller in the immobilized portion of the interface than in the rest of the interface. The flux is still smaller in the wake region.

Figure 5 shows the ratio of the wake volume to the bubble volume as a function of the cap angle for $e_e = 0.7mm$, $1.0mm$, and $1.5mm$. When the cap angle is smaller than a critical value, there is no wake. As the cap angle increases beyond the critical value, the wake volume increases

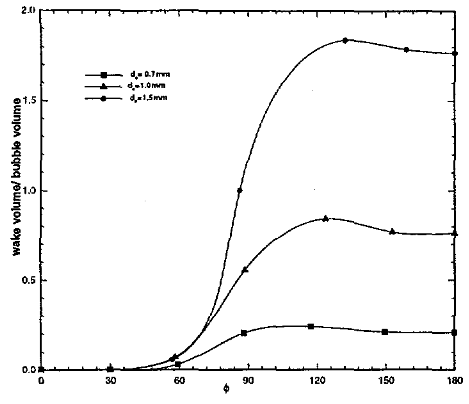

Figure 5: Ratio of the wake volume to the volume of the bubble.

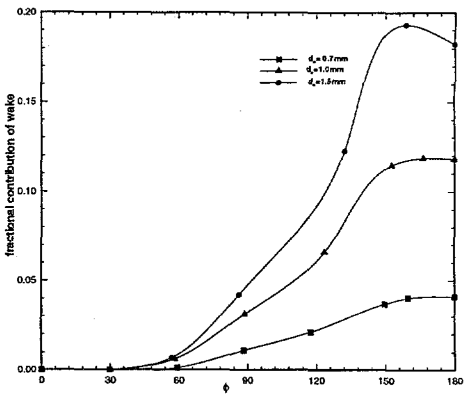

Figure 6: Contribution to the mass transfer by the wake.

rapidly and reaches a local maximum before decreasing to the value for complete immobilization. The phenomenon of a local maximum has been noted by McLaughlin [16] and Cuenot et al. [17]. On the clean portion of the surface, the tangential component of the velocity is nonzero. When the liquid encounters the surfactant cap, it is pushed away from the surface of the bubble and this appears to play a role in producing a larger wake than one would obtain with a completely immobilized surface.

Figure 6 shows the fractional contribution of the surface flux in the wake region to the Sherwood number. Results are shown for all three bubble sizes considered in this paper. The results are plotted as a function of the cap angle.

It is of interest to relate the Sherwood number to the volume concentration of surfactant. The convective-diffusion equation for the volume concentration of surfactant was not solved in this study. Therefore, it was not possible to obtain precise information about the dependence of the Sherwood number on the bulk concentration of surfactant. However, one can use the approximation in eq. (20) to relate the Sherwood number to the average volume concentration of surfactant near the bubble surface.

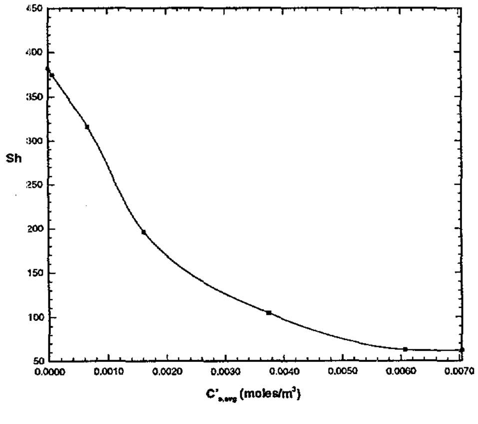

Figure 7: Sherwood number dependence on C'_s.

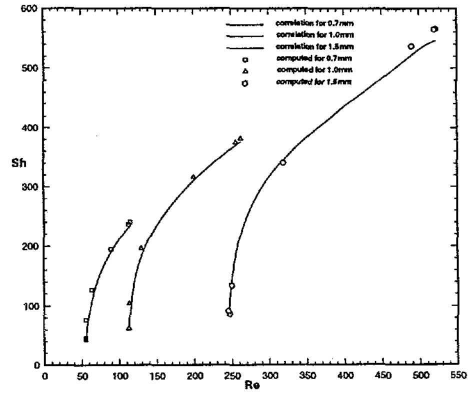

Figure 8: Comparison of Sherwood number correlation with the computed values.

The surface tension even for completely contaminated interfaces differs by only a few percent from the value for a clean surface. This justifies the use of eq. (20). Figure 7 shows the Sherwood number as a function of the average value of C_s'.

Correlation for the Sherwood number

For a bubble of diameter d_e, the Reynolds number, Re_m, and Sherwood number, Sh_m, for a clean bubble can be estimated from

$$\begin{aligned} Re_m &= -25.544 + 515.884 d_e \qquad (28) \\ Sh_m &= 1.13[1 - \frac{2.96}{Re_m^{1/2}}]^{1/2} Pe^{1/2}, \qquad (29) \end{aligned}$$

where d_e is measured in mm. The equation for Re_m is a fit to the experimental data obtained by Duineveld [18] and is valid for 0.6 mm< d_e <1.8 mm. The equation for the Sherwood number is the analytical expression derived by Lochiel & Calderbank [1].

For the completely contaminated bubble

$$\begin{aligned} Re_{im} &= \frac{Ar}{18}[1 + \frac{Ar/96}{(1 + 0.079 Ar^{0.749})^{0.755}}]^{-1} \qquad (30) \\ Sh_{im} &= 0.725 Re_{im}^{1/2} Sc^{1/3}, \qquad (31) \end{aligned}$$

where Ar, the Archimedes number, is given by $Ar = d_e^3 \rho^2 g/\mu^2$. The expression for Re_{im} was developed by Anh Nguyen [19] and the equation for Sh_{im} is a modification of the expression derived by Lochiel & Calderbank, with the multiplying constant decreased from 0.84 to 0.725 so that it fits the computed data.

The value of the Sherwood number, Sh, of a bubble with diameter d_e and Reynolds number Re can be calculated as follows:

$$\begin{aligned} x &= \frac{Re - Re_{im}}{Re_m - Re_{im}} \qquad (32) \\ y &= x^{0.434} \qquad (33) \\ Sh &= y(Sh_m - Sh_{im}) + Sh_{im} \qquad (34) \end{aligned}$$

Figure 8 compares the computed values of Sh with those obtained using the correlation.

CONCLUSION

The main results of this paper are summarized below.

- The Sherwood number, Sh, is strongly affected by the stagnant surfactant cap angle. The Sherwood number is more strongly affected by ϕ for larger bubbles in the size range considered. For cap angles smaller than about 50°, the stagnant cap has little effect on the Sherwood number. For cap angles larger than 150°, Sh is approximately constant.
- For the largest bubbles, Lochiel & Calderbank's estimate of the wake's contribution to Sh is fairly close to the computed value, but their estimate is substantially larger than the computed value for the smaller bubbles.
- The results shown are for bubbles that have risen 15cm. If the bubble rose further, the contribution by the wake would be smaller.
- Sh shows a monotonic decay with the subsurface concentration of surfactant. In all cases the surface tension varies by less than 2 % around the bubble.
- The quasisteady assumption for the bubble radius was justified by a computation of the distance needed for the radius to decrease by 10%. However surfactant sorption kinetics may introduce a strong age dependence of Sh and thus require simulation of the unsteady bubble motion.
- A correlation for Sh for bubbles in dilute aqueous solution of surfactant was presented.

ACKNOWLEDGEMENTS

This work was supported by the U.S. Department of Energy under Grant DE-FG02-88ER13919. Some of the computations were performed at the National Energy Research Scientific Computing (NERSC) Center.

REFERENCES

[1] Lochiel, A.C. and Calderbank, P.H. (1964) Mass transfer in the continuum phase around axisymmetric bodies of revolution. *Chem. Eng. Sci.* **19**, 471-484.

[2] Boussinesq, J. (1905) Calcul du pouvoir refroidissant des courants fluids. *J. Math.* **6**, 285-332.

[3] Frössling, N. (1938) Über die Verdunstung fallender Tropfen. Ger. Beit. Z. Geophysik **52** 170-216.

[4] Griffith, R.M. (1960) Mass transfer from drops and bubbles. *Chem. Eng. Sci.* **12** 198-213.

[5] Bowman, C.W., Ward, D.M., Johnson, A.I., and Trass, O. (1961) Mass transfer from fluid and solid spheres at low Reynolds numbers. *Canad. J. Chem. Engng.* **39** 9-13.

[6] Friedlander, S.K. (1957) Mass and heat transfer to single spheres and cylinders at low Reynolds numbers. *AIChE J.* **3**, 43-48.

[7] Friedlander, S.K. (1961) A note on transport to spheres in Stokes flow. *AIChE J.* **7**, 347-348.

[8] Ryskin, G. and Leal, L.G. (1983) Orthogonal mapping. *J. Comput. Phys.* **50**, 71-100.

[9] Ryskin, G. and Leal, L.G. (1984a) Numerical solutions of free-boundary problems in fluid mechanics. Part 1. The finite difference technique. *J. Fluid Mech.* **148**, 1-17.

[10] Ryskin, G. and Leal, L.G. (1984b) Numerical solutions of free-boundary problems in fluid mechanics. Part 2. Buoyancy-driven motion of a gas bubble through a quiescent liquid. *J. Fluid Mech.* **148**, 19-35.

[11] Duineveld, P.C. (1995) The rise velocity and shape of bubbles in pure water at high Reynolds numbers. *J. Fluid Mech.* **292**, 325.

[12] Haberman, W.L. and Morton, R.K. (1953) An experimental investigation of the drag and shape of air bubbles rising in various liquids. *David Taylor Model Basin, Rep.* no. 802.

[13] Haberman, W.L. and Morton, R.K. (1954) An experimental study of bubbles moving in liquids. *Proc. Am. Soc. Civ. Eng.* **387**, 227-252.

[14] Saffman, P.G. (1956) On the rise of small air bubbles in water. *J. Fluid Mech.* **1**, 249-275.

[15] Hartunian, R.A. and Sears, W.R. (1957) On the instability of small gas bubbles moving uniformly in various liquids. *J. Fluid Mech.* **3**, 27-47.

[16] McLaughlin, J.B. (1996) Numerical simulation of bubble motion in water. *J. Colloid Interface Sci.* **184**, 613-624.

[17] Cuenot, B., Magnaudet, J., and Spennato, B. (1997) The effects of slightly soluble surfactants on the flow around a spherical bubble. *J. Fluid Mech.* **339**, 25-53.

[18] Duineveld, P.C. (1994) Ph.D. Dissertation, University of Twente.

[19] Nguyen A.V. (1998) Prediction of bubble terminal velocities in contaminated water *AIChE Journal* **44** 226-230

MORE ON THE DRIFT FORCE

Graham B. Wallis

Thayer School of Engineering, Dartmouth College
Hanover, NH 03755 U.S.A.

ABSTRACT

The previous theory for the drift force on an object in an inviscid weakly rotational flow is supported by experimental data, numerical CFD experiments, and additional theoretical derivations.

INTRODUCTION

The "drift force" was introduced at this symposium three years ago by Wallis (1). Simplified analyses were presented to derive components of the force on a stationary object in a flow and were shown to be consistent with the general expression

$$\mathbf{F}_d = \rho V \mathbf{U} \cdot \underline{\underline{C}} \times \omega \quad \text{or} \quad F_{di} = \rho V \epsilon_{ikl} U_j C_{jk} \omega_l \tag{1),(2}$$

where $\mathbf{U}$ and ω are the mean incident fluid velocity and (weak) vorticity, ρ the fluid density, V the volume of the object and $\underline{\underline{C}}$ or C_{jk} the added mass tensor for the object. The drift force results from the wrapping of vortex lines around the object, their stretching, trailing and displacement in the object's wake. Because vortices move with the fluid, these displacements may be related to the "drift" of fluid particles due to the presence of the object.

Wallis claimed that the drift force should be added to the "polarization force" resulting from the interaction between the velocity gradient in the oncoming flow and flux sources that are imagined to create the object. This polarization force is

$$\mathbf{F}_p = \rho V (\mathbf{U} \cdot \nabla \mathbf{U} + \mathbf{U} \cdot \underline{\underline{C}} \cdot \nabla \mathbf{U}) \tag{3}$$

which, when added to (1), gives a net force of

$$\mathbf{F} = \rho V (\mathbf{U} \cdot \nabla \mathbf{U} + \nabla \frac{1}{2} \mathbf{U} \cdot \underline{\underline{C}} \cdot \mathbf{U}) \quad \text{or} \quad F_i = \rho V [U_j \partial U_i / \partial x_j + \partial / \partial x_i (U_j C_{jk} U_k / 2)] \tag{4),(5}$$

The present paper reports some results of three independent approaches to put these derivations on a sounder basis:

a) Experiments in a wind tunnel.

b) Numerical experiments using the CFD package FLUENT.

c) More thorough and complete analytical derivations.

EXPERIMENTS

Rife et al. (2) measured the lift force on a set of objects (Figure 1) placed in a wind tunnel (Figure 2) in which an approximately linear velocity gradient was set up by providing a suitably-varied flow resistance at the inlet to the tunnel. The lift force was measured for different values of mean velocity U, at the axis of the object, and velocity gradient, dU/dy. Results were correlated by determining the optimum coefficients, C_L and B, in an equation of the form

$$F_L = \rho V C_L U \frac{dU}{dy} + BU^2 \tag{6}$$

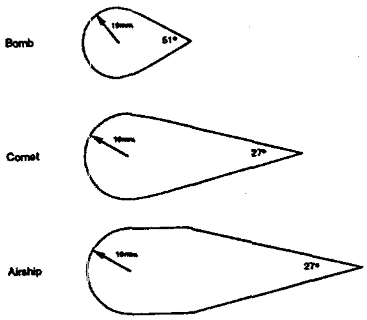

Fig. 1: Cross-section of axisymmetric objects used in the experiments.

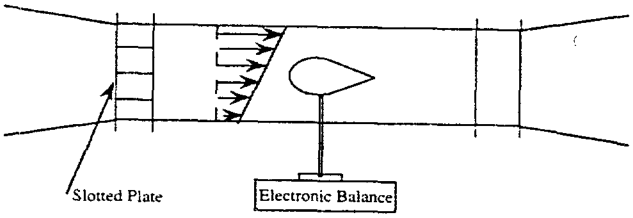

Fig. 2: An object in the wind tunnel.

B is constant for a given object and represents a small component of lift, due solely to the average flow, caused by small misalignments and asymmetries. The objects had a hemispherical nose and various forms of streamlined tail designed to achieve a separation-free flow. This is desirable in order to approximately duplicate a potential flow on which the theory depends. The "base" objects in each series are sketched in Figure 1. Larger objects with the same shapes but with volumes that were an integral multiple of the "base" volume were also tested.

The added mass coefficients were measured for these same objects by mounting them on springs, suspending them in either air or water, and recording the natural frequencies of oscillation in each case (2). Comparisons between measured lift coefficients and added mass coefficients showed substantial agreement (Figure 3).

CFD SIMULATIONS

Song (3,4) used the commercial CFD package FLUENT-UNS to simulate Rife's experiments. Besides giving predictions of the lift coefficients, these studies also revealed details of the flow structure that generally supported the mechanisms postulated in the theory.

Figure 4 shows the centerplane (z = 0) streamlines for flow around the "base" bomb in laminar shear flow. The stagnation point is lifted on the nose of the object, by the vorticity which girdles it, and there is a downwash in the wake which is symptomatic of the reaction of the lift force on the fluid. Very similar streamlines are obtained if turbulent flow is assumed. The pressure distribution on the object reveals a region of low pressure on the top side, causing an upwards lift force. In the wake, looking at the object from behind, there are two major regions of trailing vorticity, causing a strong downwash resembling what occurs behind a lifting surface such as the wing of an airplane (Figure 5).

Table 1 summarizes the lift coefficients obtained from physical experiments (2), the predictions of laminar or turbulent CFD models, and the corresponding experimentally-determined added mass coefficients. The predictions are quite good, though somewhat below the measurements. Laminar conditions (imposed in the CFD menu) generally lead to higher lift, perhaps because these conditions are closer to the theoretical assumption of inviscid flow (though the experimental conditions were turbulent). Varying the velocity gradient gave consistent values of lift coefficient. Attempts to use the RAMPANT code to model inviscid flow over these objects yielded more scatter.

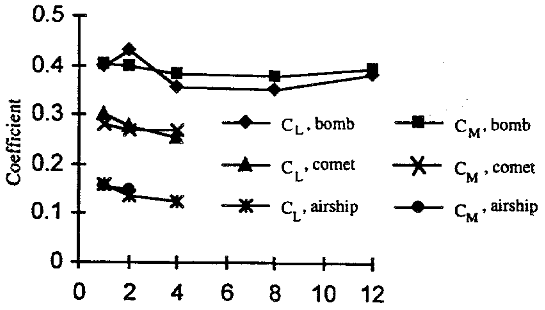

Fig. 3: Lift coefficient, C_L, in a shear flow compared with added mass coefficient, C_M, for the three objects illustrated in Fig. 1.

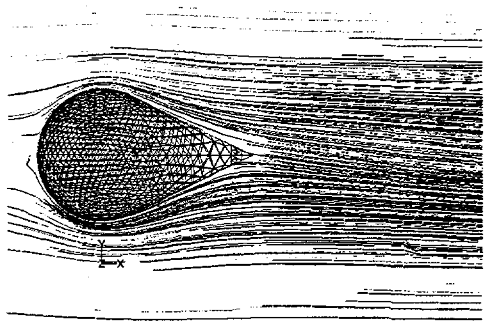

Fig. 4: Streamlines in center plane of bomb 1 in laminar flow. $\mu = 1.7894 \times 10^{-5} kg/m\dot{s}$, $\rho = 1.225 kg/m^3$

Obj.	Vol.	Lift Coefficient C_L			C_M
		Exp.	Turb.	Lam.	
Bomb	1	0.3992	0.3147	0.3631	0.402
	2	0.4278	0.3243	0.3471	0.397
	4	0.3559	0.3032	0.3199	0.381
	8	0.3526	0.3268	0.3479	0.378
	16	0.3834	0.3389	0.3538	0.396
Comet	1	0.2992	0.2080	0.2411	0.280
	2	0.2760	0.2069	0.2223	0.269
	4	0.2530	0.2304	0.2469	0.269
Airship	1	0.1613	0.1408	0.1592	0.158
	2	0.1382	0.1354	0.1520	0.149
	4	0.1231	0.1231	0.1315	N/A

Table 1: Lift coefficients obtained for all objects with both laminar and turbulent conditions ($\rho = 1.225kg/m^3$ and $\mu = 1.7894 \times 10^{-5}$)

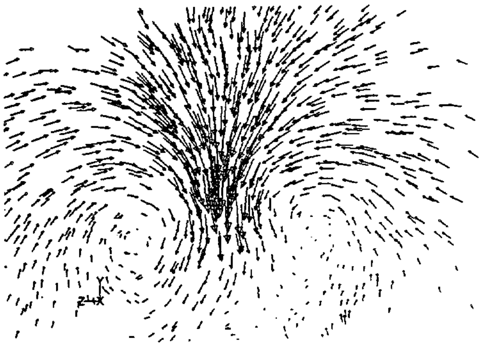

Fig. 5: y- and z-velocity components on x=370mm plane. (bomb 1 in laminar flow. $\mu = 1.7894 \times 10^{-5} kg/m\dot{s}$, $\rho = 1.225 kg/m^3$)

According to the theory of vortex line drift, the axial (x-direction) vorticity in the wake results from wrapping, or "hanging-up", of vortex lines around the object. The trailing axial vorticity can be used to derive the lift force in much the same way as the classical deduction of lift on an airplane wing. It is predicted that the moment of x-direction vorticity about the $x - y$ plane through the middle of the object is

$$\int z w_x dy dz = \frac{dU}{dy} C_{xx} V \qquad (7)$$

where C_{xx} is the principal component of the added mass tensor in the x-direction. This moment was evaluated, from data like that appearing in Figure 6, and the equivalent coefficient C_m, replacing C_{xx} in (7), computed. For three objects, e.g., Table 2, C_m extrapolates closely to C_{xx} at the $y-z$ plane at the trailing edge of the object (approximately at the location corresponding to the first row in each table) and declines with distance from the object in the wake as vorticity diffuses due to turbulent mixing and numerical diffusion.

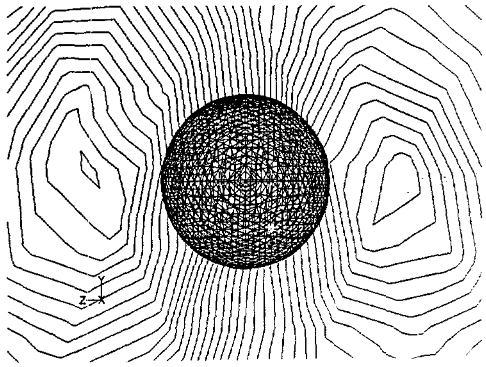

Fig. 6: x-vorticity contours on x=450mm plane. Bomb 1 in turbulent flow with inlet turbulence level of 1%, and $\bar{u} = 4m/s$, $\partial u/\partial y = 20/s$, $\rho = 1.225kg/m^3$, $\mu = 1.7894 \times 10^{-5} kg/m \cdot s$.

x (mm)	Left $\times 10^{-4}$	Right $\times 10^{-4}$	Sum $\times 10^{-4}$	Derived C_M
400	1.341	1.391	2.732	0.2899
410	1.335	1.362	2.696	0.2860
420	1.104	1.371	2.476	0.2627
430	1.272	1.115	2.387	0.2533
440	0.907	1.215	2.121	0.2233
450	0.901	1.226	2.126	0.2238

Table 2: Integral of vorticity moment in the wake. Comet in laminar flow with $\bar{u} = 4m/s$, $\partial u/\partial y = 20/s$, $\rho = 1.225kg/m^3$, $\mu = 1.7894 \times 10^{-5} kg/m \cdot s$. C_M: 0.280

THEORY

The theory has evolved considerably since its initial formulation (1). Several examples will be given:

Example I. The earlier momentum balance for a box surrounding the object did not account for the displacement of streamlines out of the sides of the box (Figure 7). A fluid particle, or vortex line, that is located on the straight side of the box has been displaced an amount **b** by the presence of the object. The amount of z-direction vorticity lost from the rectangular box on the top and bottom is then $\omega_z \int b_y ds_y$ because b_y is small. Since this reduces $\int \omega_z dV$ in the previous equation (13) it appears that (14) in the 1995 paper should read

$$\rho V C_{xx} U \omega_z - \rho U \int b_y \omega_z ds_y = \int \rho U \tilde{u}_y ds_x - \int \rho U \tilde{u}_x ds_y \tag{8}$$

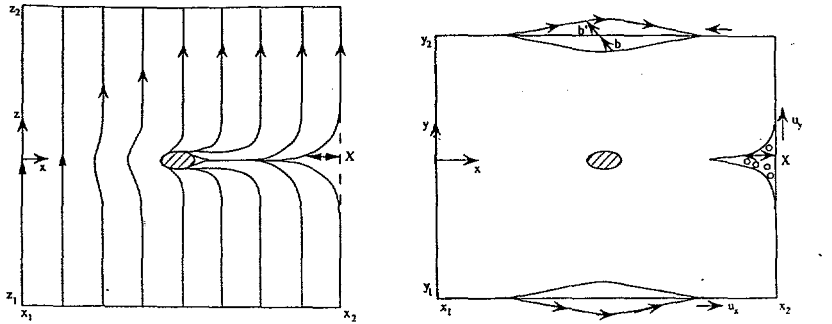

a) Vortex lines, originally in the z-direction, stretched around an object

b) Section in a z-plane, showing direction of secondary flow components at boundaries due to vorticity entrained in the wake and lost on the sides of the control volume.

Fig. 7: Control volume for Lighthill's problem.

Now Bernoulli's equation of the 1995 paper expressed the pressure perturbation solely in terms of the perturbation in $\rho v^2/2$, ignoring the fact that the stagnation pressure has also been perturbed because the streamline through the side of the box is not the same one that would be there in the unperturbed flow without the object. From Crocco's Equation the perturbation in stagnation pressure is $-\rho \mathbf{b} \cdot \mathbf{U} \times \omega$, so for U in the x-direction and ω in the z-direction, the perturbation in pressure from both the influences is

$$\tilde{p} = -\rho U \tilde{u}_x + \rho b_y U \omega_z \tag{9}$$

when (9) is used in (8) the drift force in the y-direction is again computed, as in Wallis (1995), to be

$$F_{dy} = -\rho V C_{xx} U \omega_z \tag{10}$$

The two effects that were previously neglected balance each other exactly and together have no influence on the drift force.

Example II. The sideways drift that was previously sketched qualitatively has now been computed for discs and ellipsoids at various angles of attack. A typical result is presented in Figure (8). It shows a network of fluid particles that were introduced to form a uniform mesh in the region $(-1 < y < 1), (-1 < z < 0)$ at $x = -10$. These particles flow over a circular disc of unit radius with its center at the origin and tilted at 45° to the y-axis. At the time when these particles would reach $x = 10$ if there were no disc, their positions are shown in Figure (8). Their y- and z-coordinates are almost exactly the same as they are when the same particles cross the plane $x = 10$. They represent permanent transverse displacements of streamlines in the wake.

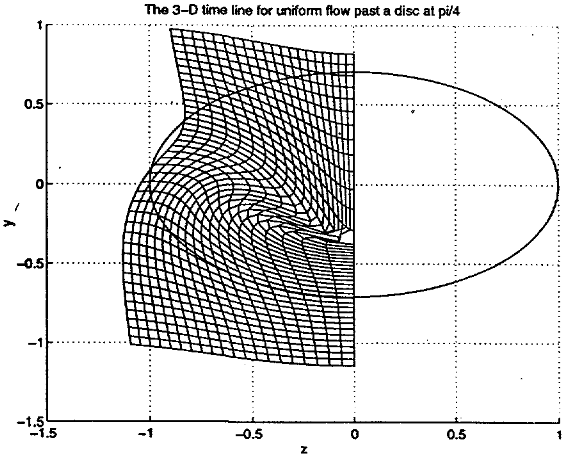

Fig. 8: Transverse drift in the wake of a tilted disc.

Displacements are generally downwards over the area indicated, inwards for positive y and outwards for negative y. The streamlines near those passing through the stagnation points are difficult to resolve, requiring a finer grid and more accurate computation.

These results have enabled us to compute and check several integrals in a general theory of drift (too extensive to present here) that also appear in a more general theory for the drift force, using a control volume of any shape. A few loose ends remain to be tied up.

Example III. At the 1995 Symposium (1) a "polarization force" was derived for an object in a potential flow with a velocity gradient. It was computed to be

$$F_p = -\rho \mathbf{D} \cdot \nabla \mathbf{U} = \rho V(\mathbf{U} \cdot \nabla \mathbf{U} + \mathbf{U} \cdot \underline{\underline{C}} \cdot \nabla \mathbf{U}) \tag{11}$$

where **D** is the polarization, or dipole moment of flux sources used to represent the object.

When the flow is not potential, the forces on the object result from interactions between the flow and both flux and circulation sources, the latter including the vortex lines that wrap around the object. The flux sources of strength ρ_m per unit volume at location r_j with dipole moment

$$D_j = \int' r_j \rho_m dV \tag{12}$$

produce a velocity which is minus the gradient of a potential

$$u_{dk} = -\frac{\partial \phi_d}{\partial x_k} \tag{13}$$

The component of the force that is due only to the interaction between these flux sources and the unperturbed flow is evaluated from a large control volume around the object:

$$\int \left(r_j \frac{\partial U_k}{\partial x_j} u_{dk} ds_i - r_j \frac{\partial U_i}{\partial x_j} u_{dk} ds_k - r_j \frac{\partial U_k}{\partial x_j} u_{di} ds_k \right) \tag{14}$$

The surface integrals may be evaluated by converting to volume integrals and treating the flux sources as distributed. The factor of $\partial U_i / \partial x_j$ is

$$\int r_j \frac{\partial \phi_d}{\partial x_k} ds_k = \int \frac{\partial}{\partial x_k} \left(r_j \frac{\partial \phi_d}{\partial x_k} \right) dV$$

$$= \int \left(\frac{\partial \phi_d}{\partial x_j} + r_j \frac{\partial^2 \phi_d}{\partial x_k^2} \right) dV = \int \left(\frac{\partial \phi_d}{\partial x_j} - r_j \rho_m \right) dV = \int \phi_d ds_j - D_j \tag{15}$$

and the factor of $\partial U_k / \partial x_j$ is

$$\int r_j u_{dk} ds_i - r_j u_{di} ds_k = \int \left[r_j \left(\frac{-\partial^2 \phi_d}{\partial x_k \partial x_i} + \frac{\partial^2 \phi_d}{\partial x_i \partial x_k} \right) + \frac{\partial r_j}{\partial x_k} \frac{\partial \phi_d}{\partial x_i} - \frac{\partial r_j}{\partial x_i} \frac{\partial \phi_d}{\partial x_k} \right] dV$$

$$= \int \left(\delta_{jk} \frac{\partial \phi_d}{\partial x_i} - \delta_{ij} \frac{\partial \phi_d}{\partial x_k} \right) dV = \delta_{jk} \int \phi_d ds_i - \delta_{ij} \int \phi_d ds_k \tag{16}$$

Therefore, (14) may be expressed as

$$\frac{F_i}{\rho} = -D_j \frac{\partial U_i}{\partial x_j} + \frac{\partial U_j}{\partial x_j} \int \phi_d ds_i + \left(\frac{\partial U_i}{\partial x_j} - \frac{\partial U_j}{\partial x_i} \right) \int \phi_d ds_j \tag{17}$$

The first term in (17) leads to the "polarization force" obtained earlier in (11). The second term vanishes in an incompressible flow. The final term is proportional to the vorticity and to a surface integral that depends on the choice of control volume. Since the net force is independent of such a choice, there must be a compensating term from other components of the force, involving particle and vortex line displacements due to "drift".

Example IV. An alternative representation of the object is by circulation sources wrapped around its surface to account for the velocity jump between the solid and the surrounding fluid. Consider one of these vortex loops of strength $d\Gamma$ described by the vector location $\mathbf{r}$ (or r_k) of points along it. The "lift force" on an element of this ring due to interaction with the unperturbed flow might be expected to be

$$\mathbf{dF} = \rho(\mathbf{U} + \mathbf{r} \cdot \nabla \mathbf{U}) \times \mathbf{dr} d\Gamma \tag{18}$$

When this is integrated along the entire ring the first term on the right hand side vanishes because $\int \mathbf{dr} = 0$. The remaining term, in index notation, is

$$\frac{dF_i}{\rho d\Gamma} = \int r_j \frac{\partial U_l}{\partial x_j} dr_k \epsilon_{ilk} \tag{19}$$

and the z-component is explicitly

$$\frac{dF_z}{\rho d\Gamma} = \frac{\partial U_x}{\partial x}\int x dy + \frac{\partial U_x}{\partial y}\int y dy + \frac{\partial U_x}{\partial z}\int z dy - \frac{\partial U_y}{\partial x}\int x dx - \frac{\partial U_y}{\partial y}\int y dx - \frac{\partial U_y}{dz}\int z dx \tag{20}$$

Now, for integration around the entire vortex loop we have

$$\int x dx = \int y dy = \int z dz = 0, \qquad \int (x dy + y dx) = \int d(xy) = 0 \qquad (21),(22)$$

and hence

$$\int x dy = -\int y dx = \frac{1}{2}\int (x dy - y dx) \tag{23}$$

with similar expressions in the other directions.

Also, by definition

$$\nabla \cdot V = \frac{\partial U_x}{\partial x} + \frac{\partial U_y}{\partial y} + \frac{\partial U_z}{\partial z}, \qquad \omega_y = \frac{\partial U_x}{\partial z} - \frac{\partial U_z}{\partial x}, \qquad \omega_x = \frac{\partial U_z}{\partial y} - \frac{\partial U_y}{\partial z} \qquad (24),(25)$$

Using (21) through (25) in (20) we obtain

$$\begin{aligned} \frac{2dF_z}{\rho d\Gamma} = \int (x dy - y dx)\left(\nabla \cdot V - \frac{\partial U_z}{\partial z}\right) + \int (z dy - y dz)\left(\omega_y + \frac{\partial U_z}{\partial x}\right) \\ + \int (z dx - x dz)\left(\omega_x - \frac{\partial U_z}{\partial y}\right) \end{aligned} \tag{26}$$

which is the z-component of

$$\nabla \cdot V \int \mathbf{r} \times \mathbf{dr} + \omega \times \int \mathbf{r} \times \mathbf{dr} - \left(\int \mathbf{r} \times \mathbf{dr}\right) \cdot \nabla U \tag{27}$$

Now, Cai and Wallis (6) showed that the dipole moment of a stationary object in a flow can be expressed as

$$\mathbf{D} = \frac{1}{2}\int \mathbf{r} \times \mathbf{dr}\, d\Gamma \tag{28}$$

and therefore (19) integrated over the entire object yields

$$\frac{\mathbf{F}}{\rho} = (\nabla \cdot \mathbf{V})\mathbf{D} + \omega \times \mathbf{D} - \mathbf{D} \cdot \nabla \mathbf{U} \tag{29}$$

The first term vanishes in an incompressible fluid. The second term may be expanded (6),

$$\mathbf{D} = -\underline{\underline{D}} \cdot \mathbf{U}V = -\left(\underline{\underline{I}} + \underline{\underline{C}}\right) \cdot \mathbf{U}V \tag{30}$$

to give the drift force $\rho V\mathbf{U} \cdot \underline{\underline{C}} \times \omega$ together with an additional term $\rho VU \times \omega$ that would result if the object "froze" the unperturbed vorticity threading it. This might be justified by the argument that the representation of the object by vortex rings does indeed reduce the velocity inside it to zero, whereas the "model" using flux sources sweeps the ends of the internal vortex rings to the rear stagnation point whence they stretch along a long filament to join their remaining lengths far in the wake. The final term is the polarization force in (11) that also appeared in (17).

The point of examples III and IV is that partial superpositions yield some of the desired forces and are only consistent when there is no vorticity in the main flow. A complete formulation should consider the effect of the displacement of the external vortex lines as well.

REFERENCES

1. G.B. WALLIS, "The Drift Force on an Object in an Inviscid Weakly-Varying Rotational Flow," Presented at the Thirteenth Symposium on Energy Engineering Sciences, Argonne National Laboratory, May (1995).
2. J. RIFE, J. HE, Y. SONG, and G.B. WALLIS, "Measurements of the Drift Force," *Nuc. Eng. Design*, **175**, 71-76 (1997).
3. Y. SONG, "Numerical Study of Drift Force on Objects in Sheared Flow," M.S. Thesis, Thayer School of Engineering, Dartmouth College, March (1998).
4. Y. SONG and G.B. WALLIS, "Numerical Study of Drift Force on Objects in a Shear Flow," Presented at the Third International Conference on Multiphase Flow, ICMF'98, Lyon, France, June 8-12 (1998).
5. G.B. WALLIS, "Polarization of an Object in a Potential Flow: Some Theorems and Applications to Ellipsoids," *Advances in Multiphase Flow*, Eds. A. Serizawa, T. Fukano, J. Bataille, Elsevier Science B.V., 185-189 (1995).
6. X. CAI and G.B. WALLIS, "The Added Mass Coefficient for Rows and Arrays of Spheres Oscillating Along the Axes of Tubes," *Physics of Fluids A*, **5**(7), 1614-1629 (1993).

SIMULTANEOUS SMALL ANGLE NEUTRON SCATTERING AND RHEOMETRIC MEASUREMENTS ON A DENSE COLLOIDAL SILICA GEL

Howard J.M. Hanley, Chris D. Muzny and Brent D. Butler

Physical and Chemical Properties Division,
National Institute of Standards and Technology[1],
Boulder, CO 80303

ABSTRACT

Small angle neutron scattering (SANS) intensities, from a dense (volume fraction 0.17) colloidal 7 nm silica gel, were measured as a function of the scattering wave vector and of time for systems gelled statically and gelled in the presence of an applied constant strain rate. The viscometric behavior of the system was measured simultaneously. The substantial differences between the structure of the gel formed statically and under shear are discussed. The effective hydrodynamic diameters of the aggregated components of the gel were estimated by dynamic light scattering.

INTRODUCTION

We present small angle neutron scattering (SANS) data from a dense solution of colloidal silica gelling under an applied shear rate. The key data are the time dependence of the scattered intensity $I(q,t)$ as a function of the wave vector q (where for neutrons of incident wave length λ, $q = (4\pi/\lambda)\sin(\theta/2)$ with θ the angle between the incident and scattered neutron beams) and the corresponding shear viscosity η, and shear stress τ. This is a pioneering experiment. Our interest here is to see how shear affects the gelation mechanism and the structure of the final gel, but the procedure has wider implications. For the first time, it is possible to measure SANS structural and

---

[1] Publication of the National Institute of Standards and Technology, not subject to copyright in the USA.

viscometric data simultaneously because we have recently adapted a commercial constant stress rheometer to couple with the 30 m SANS spectrometers at the NIST Cold Neutron Research Facility (NCNR) [1].

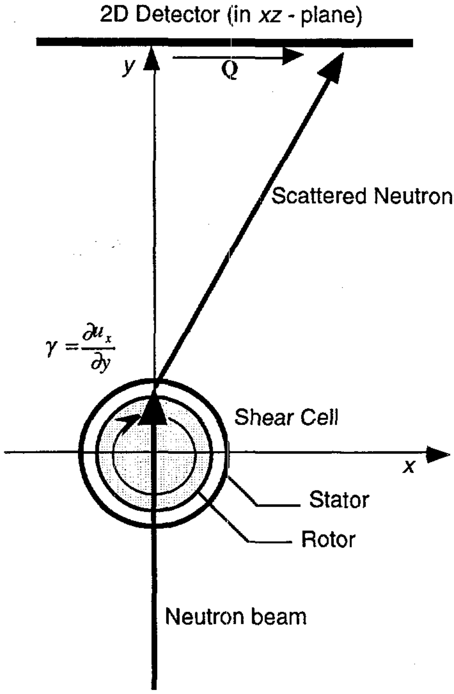

Figure 1. Beam path through the rheometer modified for SANS experiments.

Figure 1 shows schematically the beam path through the instrument which is set up in a Couette shearing mode with the sample (volume approximately 7 ml) contained in the annular gap between an inner cylinder (rotor) and a stationary outer cup (stator). The gap width is set at 0.5 mm or 1 mm by the appropriate choice of a rotor-stator pair. For these experiments, the beam was incident along the y–axis and the scattered intensity recorded on a SANS two-dimensional detector placed in the xz–plane. Scattering from a gelling silica sample was measured with the system at rest, and when subjected to a constant applied shear rate, $\gamma = du_x/dy$. Here, the flow velocity of the sample is in the x–direction, u_x. The rheometer operations and SANS output are linked and synchronized through a personal computer.

SAMPLE PREPARATION AND SANS SET-UP

All the experiments were carried out on gels made from a common stock of commercial grade Ludox SM-30 [2] – a stable aqueous colloidal silica suspension at pH = 9.8. The silica spheres were designated by the manufacturer to have a nominal diameter $\sigma = 7$ nm with an estimated 20% polydispersity. We determined the suspensions were 31% by mass SiO_2 (corresponding to a volume fraction $\phi = 0.17$) with a suspension density $\rho = 1.215$ $g \cdot cm^{-3}$.

Sols were prepared by filtering the suspension through 0.45 μm membrane filters. Concentrated HCl was added to the sol until the pH was lowered sufficiently to initiate gelation. For convenience, we required that the time scale of our SANS experiments was such that the gel point was about 60-90 min after initiation, and that a final gel formed after about 8 h. Hence, for a typical experiment, 140 ± 3 μl of concentrated HCl (12 $mol \cdot dm^{-3}$, $\rho = 1.186$ $g \cdot cm^{-3}$) were added to 12.15 g of the filtered sol (10 cm^3), and the resulting mixture was vigorously agitated for about 30 s. The initial pH of the gelling mixture was measured to be 8.02 ± 0.02 and was found not to change noticeably during the gelation process.

The SANS experiments were carried out on the 30 m SANS NG7 spectrometer configured with an incident neutron wavelength $\lambda = 0.7$ nm and a sample-detector distance of 13.6 m with a 0.25 m offset, giving a wave vector range of $0.03 < q$ $(nm^{-1}) < 1.2$. The scattered neutrons were detected on the instrument's 2D position sensitive detector and the scattered intensities, $I(q,t)$ measured as a function of time t. We detected no anisotropy in the scattered intensity pattern, so the measured counts were azimuthally averaged and these averaged intensities were corrected for empty cell and solvent scattering in the usual way and placed on an absolute scale by normalizing to the intensity of a water standard [3].

After gel initiation the sample was placed immediately into the Couette cell of the modified rheometer. After loading, the rheometer was set to apply a constant applied shear rate, and the SANS intensities and viscometric data, specifically the shear viscosity, recorded as a function of time. The counting intervals were selected to be consistent with the viscosity variation of the gelling sample. Data were collected and averaged over 5 min intervals at times up to and just beyond the gel point, and collected and averaged at 20-30 min intervals for, at least, another 4 h, or until the scattered intensities became essentially time-independent. Thermostatting was ambient at 25 ± 2 ^{o}C. Some data were recorded with the rheometer in constant stress mode, but the majority of data were taken when the sample was subjected to a constant shear rate of 244 s^{-1}, 533 s^{-1} and 1645 s^{-1} with a Couette cell gap width of 0.5 mm. Additional runs with a cell gap width of 1 mm were carried out on selected samples.

RESULTS

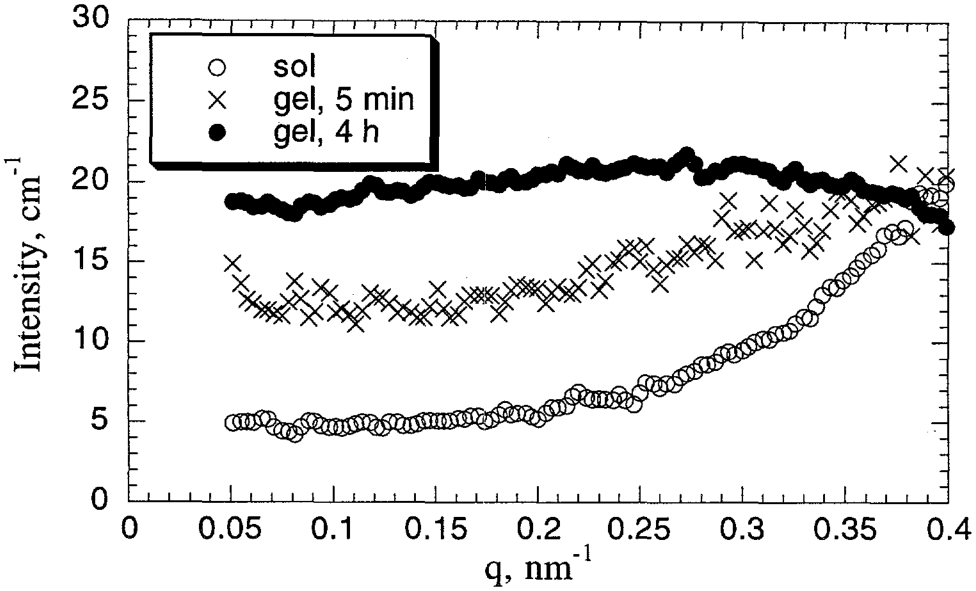

Figure 2: SANS intensity curves showing the time variation of the static colloidal silica gelling system compared with curve for the sol.

Figure 2 shows three curves of the scattered intensity from the static (that is, non-sheared) system as a function of time: at zero time when the system is the precursor suspension or sol, and at 5 min and 4 h after gel initiation. The rise in intensity for the sol near $q = 0.4$ nm^{-1} results from scattering between the sol particles (spaced about 16 nm apart). At very early times after gel initiation, this particle-particle separation peak disappears because the addition of HCl increases the screening of the charged colloidal spheres, hence decreasing their effective interaction diameter and the effective volume fraction of the particles. Also, shortly after gel initiation, a less intense peak appears at higher q (~ 0.8 nm^{-1}, not shown in the figure) which represents particle-particle contact at about 7 nm.

The onset of the clustering that characterizes the gelled state is represented by the rise in scattering power at low q. As time progresses the low-q scattering continues to increase indicating coarsening of the clusters. At later times a peak in this low angle scattering (shown here at approximately $q = 0.2$ nm^{-1} after 4 h) can be identified and its location can be used as a rough measure of the cluster-cluster correlation distance; ~ 20 nm.

As observed previously, the low-q scattering is substantially enhanced in a system under shear [4]. Figure 3 displays the scattered intensity from the gel at 4 h after gelation when the system was subjected to a constant shear rate $\gamma = 533\ s^{-1}$. For times longer than 4 h, the intensity at low q increases slowly with time until it remains essentially static after 8 h. It is important to note that this long-time intensity curve does not change noticeably after the shear is turned off. Similar results were obtained from the gel at other shear rates.

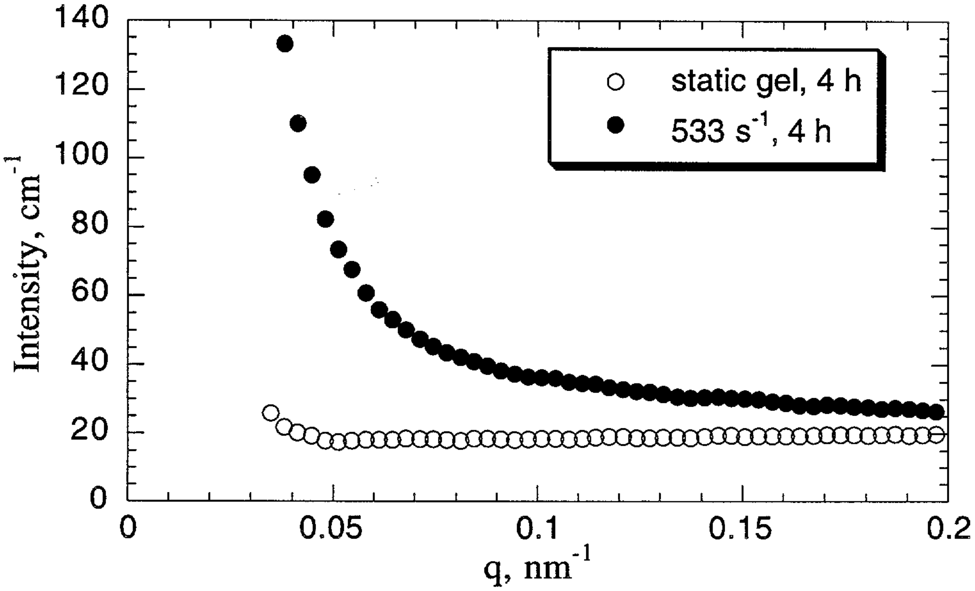

Figure 3: SANS intensity curve from the system 4 h after gel initiation compared with the curve from the system gelled statically.

We now examine the juxtaposition of the time-dependent scattered intensities measured from the sheared system with the behavior of the viscosity measured simultaneously. If the system is subjected to a low constant shear stress, and then gelation is initiated, the viscosity will increase until, at a time designated the gel point time, the viscosity becomes that of the solid. If, instead, the system is subjected from initiation to a constant shear rate the viscosity peaks at a time roughly equal to the gel time of an unsheared gel, but then the viscosity falls to an asymptotic value that is higher than that of the initial sol but much lower than the peak viscosity. *The state of the sol at this asymptotic time is not that of a 'broken' gel, or a gel that has separated from the container walls due to the high shear stress near the gel point (as one might suspect), but, rather is that of a bulk fluid whose viscoelastic properties have been somehow altered by the application of a shear.* Figure 4 shows the viscosity/intensity time variation for the gelling system subjected to a shear of 533 s^{-1} at $q = 0.048\ nm^{-1}$. Note; (a) the correlation between the maximum in the viscosity and a jump in $I(q,t)$ and (b) the increase in $I(q,t)$ with t (to reach a plateau value at long time) yet the system is liquid-like.

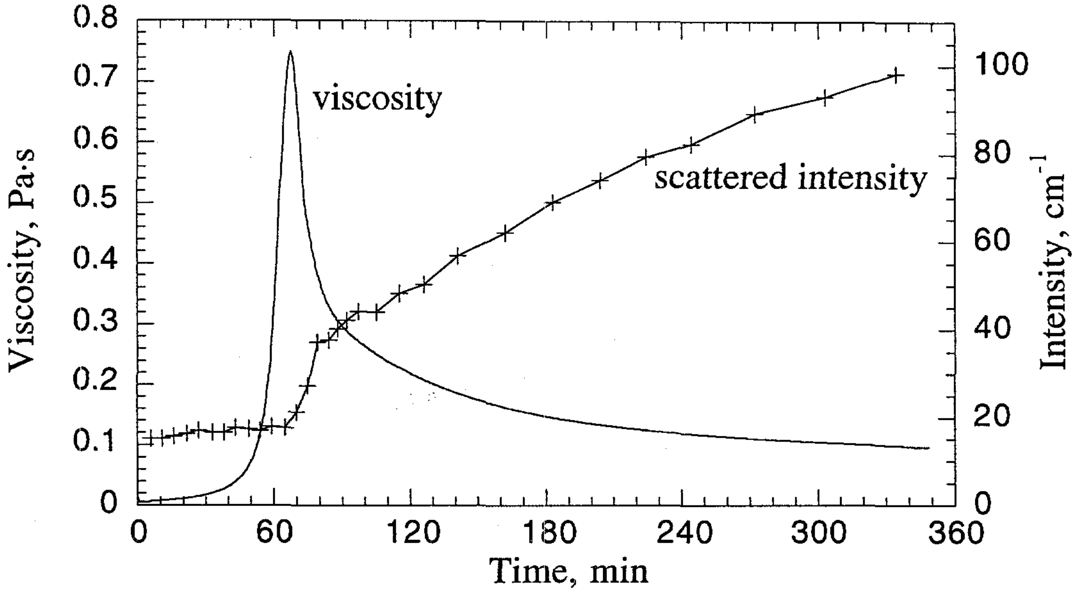

Figure 4. Variation of the viscosity coefficient with time for the system subjected to a constant shear rate of 533 s^{-1}. Superimposed is the scattered intensity measured as a function of time at $q = 0.048$ nm^{-1}. Both the viscosity and intensity were measured simultaneously.

Patterns similar to Figure 4 were seen for systems subjected to other shear rates. We will state here, and discuss in a future paper, the observation that in each case, although the peak viscosities were different, the shear stresses on the sol at the peaks were nearly identical. A critical stress value is thus likely an important parameter for describing gelation under shear.

Hydrodynamic diameters. An understanding and interpretation of the behavior of the scattering is a subject of an ongoing investigation and further results will be discussed later. We, however, wished to determine if the dramatic change in $I(q,t)$, at times corresponding to the gel point time results primarily from the growing size of the clusters or from a sudden change in the cluster ordering. Accordingly, for selected gelation runs, samples of the system were extracted and diluted at various times after gel initiation and the diluted samples were investigated by SANS and by dynamic light scattering. About 0.05 ml of the gelling system was extracted from the Couette cell at various times after gel initiation and added to 10 ml of deionized water. The diluted sample was sealed in conventional cells and the dynamic light scattering correlation function and the SANS intensities were measured; the hydrodynamic size and a Guinier radius of gyration of the clusters could thus be determined. For the sheared system, we found that the diameters were close to the equivalent diameters of the static gel for times up to the gel point, but then they increase dramatically by about a factor of 30. This sharp increase in diameter corresponded with the discontinuity in the intensity - and hence with the viscosity maximum and critical stress. Thus, it is clear that the sharp rise in intensity near the peak value results primarily from a sudden change in the cluster size, not from ordering. An additional interesting observation is that the aggregated particles in these diluted samples decomposed in a few days until their sizes became roughly equal to the particle diameters found in the initial sol – an unexpected result that indicates that the aggregation of colloidal silica is reversible.

CONCLUSIONS

The objective of this short paper is to report on the data only; interpretation is minimal and a more complete discussion will be forthcoming. We conclude, therefore, by highlighting some of the results obtained:

1. Substantial differences in the low q behavior of $I(q,t)$ are observed between gels formed statically and gels formed under a constant shear rate. In general, $I(q,t)$ increases at low wave vectors as the gelation reaction proceeds, but, the increase is enhanced substantially when gelation occurs in the presence of an applied shear.
2. Under static conditions, the shear viscosity increases as a function of time after gel initiation and then diverges when the gel becomes solid. By contrast, under a constant shear, the gelling system's viscosity increases initially, but, after a time corresponding to the gel point time, the viscosity decreases to an asymptotic value that is higher than that of the initial sol but lower than the peak value.
3. At different shear rates, the viscosity at the peak is different, but, the shear stress at the peak is approximately independent of shear rate. A critical shear stress is thus observed.
4. The time at which the critical stress, and the equivalent viscosity maximum, is reached corresponds to a substantial and discontinuous enhancement in the low-q scattering.
5. Throughout the shear-influenced gelation, the system remains liquid-like in that it flows. On removing the shear, the viscosity increases with time and the gel sets to a solid, yet the structure of the material, measured by the SANS intensity patterns, does not change during this setting process.
6. Samples from the system were extracted at various times after gel initiation. Dilute aqueous solutions of the extracts were prepared, and characteristic effective particle diameters were estimated by SANS and by dynamic light scattering. We found that the diameter increased dramatically at a time corresponding to the jump in the scattered intensity. The isolated particles formed under shear, however, they decomposed into units of size equal to the particle size found at gel initiation, leading one to surmise that a colloidal silica gel is

reversible.

Finally, we remark on the technological implications of the results presented here. As far as we are aware, it was not previously known that a silica sol, which has had its pH altered so as to initiate gelation, could be held indefinitely in the fluid state by the application of a constant shear. Apparently, there are no irreversible chemical reactions that prevents the normal formation of a gel once this shear is removed. This implies that production of materials using the sol-gel process might be accomplished via a continuous casting process instead of the currently used batch process mode. Such shifts in technology in other materials industries (steel, for example) have reduced manufacturing costs markedly. It is, therefore, important to understand the structural changes that take place in the asymptotic regime of Fig. 4 that may impact a gel made from this pre-sheared sol. Investigation along these lines continues.

ACKNOWLEDGEMENT

This work was supported by a grant from the Division of Engineering and Geosciences, Office of Basic Energy Sciences, U.S. Department of Energy. The comments of John Bartlett and Elizabeth Drabarek of the Australian Nuclear Science and Technology Organisation are much appreciated.

REFERENCES

1. G.C. STRATY, C.D. MUZNY, B.D. BUTLER, M.Y. LIN, T. SLAWECKI, C.J. GLINKA and H.J.M. HANLEY, "A Rheometric Shearing Apparatus at the NIST Center for Neutron Research (NCNR)," *Nucl. Instr. and Methods in Phys. Res.* (in press).
2. The trade name is noted to identify the product. Use of this material does not imply endorsement by NIST.
3. C.J. GLINKA, J.G. BARKER, B. HAMMOUDA, S. KRUEGER, J.J. MOYER and W. J. ORTS, "The 30 m Small-Angle Neutron Scattering Instruments at the National Institute of Standards and Technology," *J. Appl. Cryst.* 31, (in press).
4. C.D. MUZNY, G.C. STRATY and H.J.M. HANLEY, "Small Angle Neutron Scattering Study of Dense Sheared Silica Gels," *Phys. Rev.E* 50, 675 (1994).

TURBULENT TRANSPORT PROCESSES ACROSS INTERFACES

V. De Angelis and S. Banerjee

Department of Chemical Engineering
University of California Santa Barbara
Santa Barbara, California

ABSTRACT

Experimental and numerical investigations of turbulent structure near the interface between two flowing streams indicate qualitative similarity to those in wall turbulence – if the shear rates correspond. There are detailed differences, which depend on the interfacial tension, fluid densities and viscosities for the gas and liquid streams. At atmospheric conditions, and restricting consideration to the wave scales important for scalar transfer (capillary waves), the differences are primarily on the liquid side. The liquid-side tangential turbulent fluctuations peak right at the interface, whereas on the gas side they peak a small distance away – much like in wall turbulence. In some sense, the liquid therefore sees the interface much like a slip surface, whereas the gas sees it much like a wavy solid wall. Furthermore, the patterns of shear stresses and pressure are primarily controlled by the quasi-streamwise vortical structures on the gas-side, with their associated sweeps and ejections. Quasi-streamwise vortices also arise near the interface on the liquid side, but the associated sweeps and ejections do not correlate with the interfacial shear stress pattern. Low-speed-high speed streaky regions are also seen near the interface on both sides, with their spanwise spacing scaling with kinematic viscosity and friction velocity (defined for each side as the square root of the ratio between the interfacial shear stress and the fluid density). Ejection and sweep frequencies also scale with the same parameters.

Turning now to heat and mass transfer mechanisms, they are primarily controlled by the sweeps, with ejections playing an important role in a certain range of Schmidt numbers on the gas side. An understanding of the dominant mechanisms allows a simple parametrization of the scalar transfer velocity on each side, which compares well with experiments and direct numerical simulations. Capillary waves appear to have little effect on the parametrizations for scalar transfer velocity.

INTRODUCTION

Turbulence structure at boundaries govern high Reynolds number transport processes and must be elucidated for applications in the process and power industry, as well as in several atmospheric and environmental problems. A number of investigations have dealt with the phenomena that occur near solid boundaries. Work by Kline et al[1] and many others have shown that streaks of low-speed/high-speed fluid form near the wall, and that these break down periodically in a spectacular phenomenon called a "burst", in which fluid is ejected from the wall layer with significant wall-normal velocities. These "ejections", and the associated "sweeps" that follow account for nearly 80% of the Reynolds stresses observed in boundary layers. Typical spanwise spacing of the streaks are $\lambda_w^+ \sim 100$, where λ_w^+ is the non-dimensional spanwise spacing – the non dimensionalizing variables being the shear velocity, $u_{\tau w} = \sqrt{\tau_w/\rho}$ and the kinematic viscosity, ν. Rashidi and Banerjee [2], amongst others, have shown that, at sufficiently high Reynolds number, inner variables give a non-dimensional time between bursts $T_{\tau w} = (u_{\tau w}^2/\nu)\overline{T}_w \sim 90$.

In contrast to this understanding of the main features of turbulence near solid boundaries, albeit with many outstanding questions regarding the reasons for the phenomena, very little was known about turbulence near fluid-fluid boundaries till recently. This, in spite of the importance of near-interface phenomena in determining mass and heat transfer rates in a variety of contacting equipment like gas absorbers and condensers, as well in geophysical problems like gas transfer at the air-sea interface.

We do know that at fluid-fluid interfaces the mass transfer coefficient, β, varies as the $1/2$ power of the molecular diffusivity, D, whereas at solid boundaries β varies roughly as the $2/3$ power of D. Obviously molecular effects are more important at solid boundaries, where turbulence is damped more than it is near clean, mobile interfaces.

The present study complements earlier experimental work by Rashidi and Banerjee[2] and is aimed toward a better understanding of such phenomena via direct numerical simulation (DNS), *i.e.* solving the full time-dependent 3-D Navier-Stokes equations without any closure model. This DNS aims to calculate the mean statistical properties of turbulence on both sides of the near-interface region, clarify mechanisms related to the coupling fluxes between the phases, with particular regard to the role of turbulence structures (*i.e.* their appearance and evolution in the immediate neighborhood of the fluid-fluid interface) and to develop scalar transfer parametrizations based on the physical insight gained from the DNS.

It can be shown that scalar transfer occurs over scales that are at most affected by capillary waves. It therefore becomes possible to examine the controlling processes by DNS over a domain size of the order of several capillary waves, and in isolation from surface deformations that are larger in scale.

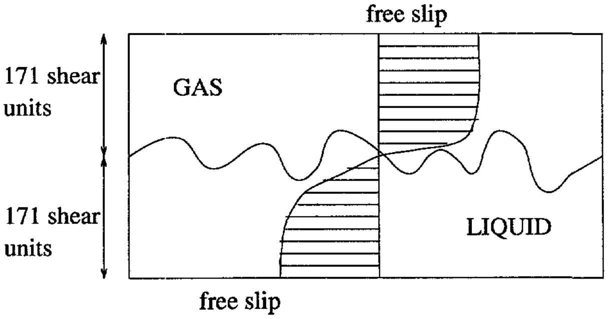

Figure 1: Geometry of the Simulation

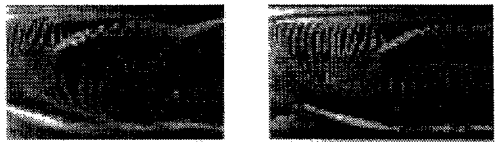

Figure 2: Bursts from the liquid surface for counter-current flow

The typical flow geometry, investigated as a canonical problem is shown in Figure 1. Gas flows co- or counter-current to the liquid flow. The interface for moderate wind speed, ~O(3-6 m/s), forms capillary waves that have amplitude of roughly a millimeter. Before discussing the effect of waves, however, we examine the turbulence structures on the liquid and gas side in the simpler situation in which the interface is kept flat.

2. GAS-LIQUID FLOW ACROSS FLAT GAS-LIQUID INTERFACES

Consider now experimental conditions set to keep the liquid Froude number low and the gas velocity low enough to be well away from Kelvin-Helmhotz instabilities. A non-wavy surface can be obtained even when quite high shear rates are imposed, as shown by Rashidi and Banerjee[2].

They visualize the liquid side flow, using a microbubble tracer technique, in a situation in which there is a wall at the bottom of the liquid stream. The high-speed, low-speed streaks seen by many investigators are found near the wall. However similar structures are also seen at high enough shear rates at the interface – whereas at low shear rate the interface structure looks patchy. Clearly there is a shear rate at which transition occurs, but once streaks are established in the near interface region, the similarity between the bursts seen in the vicinity of the wall and of the interface is remarkable. This is shown in Figure 2, representing a side view of the liquid stream, with gas on the top going counter-current to the liquid.

Quantitative similarities were also found by Rashidi and Banerjee[2]. If the interfacial streak spacing is non-dimensionalized with the interfacial shear rate, then $\lambda_I^+ \sim 100$, where $\lambda_I^+ = \lambda_I u_{Ti}/\nu$. Thus the interfacial streak spacing scales in the same way as the wall streak spacing, provided one uses the interfacial shear stress to obtain the velocity scale. Furthermore the period between bursts is seen to scale in the same way as at the wall, i.e. $\overline{T}_{BI}^+ \cong 90$.

Even if the qualitative picture seems the same at a sheared interface and at a solid boundary, there are detailed differences between the two cases that will play a role in mass and heat transfer processes.

Lombardi et al.[3] did a simulation assuming a flat interface. They resolved about 170 shear-based units, h^+, on each side of the interface, where h^+ is based on the interfacial shear velocity, u_{Ti}.

Runs at different density ratios (R^2) between the fluids were performed. The gas and liquid were coupled through continuity of velocity and stress boundary conditions at the interface.

The interfacial plane itself showed regions of high shear stress and low shear stress, with low shear stress regions corresponding to the low speed regions and the high shear stress to the high speed regions. The low shear stress regions are streaky in nature with high shear stress islands. At the edges of the high shear stress regions, vortices are seen to spin up on both sides of the interface. These are initially in the plane normal to the interface but subsequently are stretched in the quasi-streamwise direction by the mean flow. These quasi-streamwise vortices are known to play a major role in the ejection-sweep processes observed in wall turbulence, and they do the same at the gas-liquid interface.

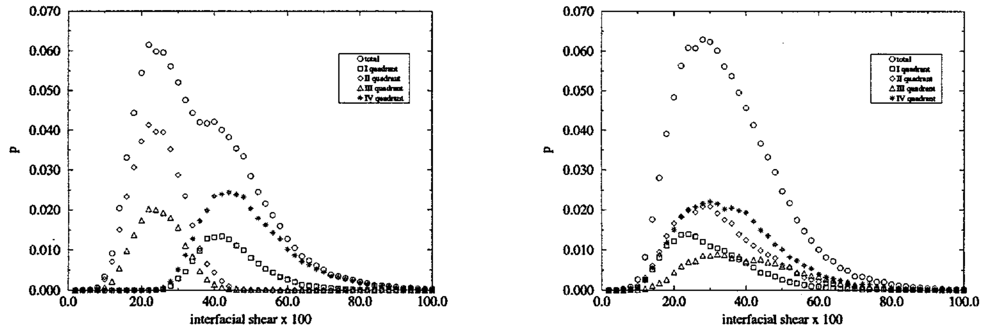

Figure 3: Probability of strongly coherent events classes according to quadrant as a function of interfacial shear stress in the region over which the events occur. left: gas; right: liquid

At this point it is worth considering how the high shear stress regions form. This can be clarified by considering a quadrant analysis of the velocity field over the interface in which velocity fluctuations in each quadrant of the Reynolds stresses are correlated with shear stress at the interface. In the first quadrant both the streamwise and interface normal velocity fluctuations are positive. In the second, the streamwise component is negative but the interface normal component is positive. This corresponds to an ejection of low speed fluid. In the third quadrant both the streamwise and the interface-normal velocity fluctuations are negative, and in the fourth the streamwise component is positive whereas the interface-normal component is negative. The fourth quadrant then corresponds to a sweep in which high-speed fluid is brought towards the interface. Consider now the correlation of each quadrant of such velocity fluctuations with the interfacial shear stress shown in Figure 3 (left) on the gas side. It is clear that sweeps, i.e., in the fourth quadrant, lead to the high shear stress regions whereas ejections lead to the low shear stress regions. This is what is observed in wall turbulence at a solid boundary and therefore the gas sees the liquid surface much like a solid boundary.

However, if we look at Figure 3 (right), it is immediately clear that no such correlation exists on the liquid side. In fact, all the quadrants have similar behavior with regard to the shear stress regions that occur below the high speed sweeps on the gas side, *i.e.* , the motions that bring high speed fluid from the outer regions to the interface on the gas side, lead to the high shear stress at the interface. Conversely, ejections on the gas side which take low speed fluid away from the interface into the outer flow, strongly correlate with low shear stress regions. The liquid does not behave in this way and does not dominate the pattern of shear stress on the interface.

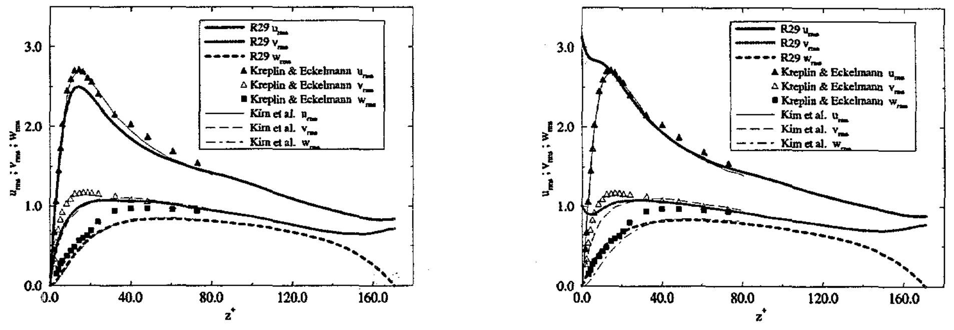

Figure 4: Results from direct numerical simulation on rms velocity fluctuations, left: gas; right: liquid

The difference between the gas and the liquid phases in the near interface region is further clarified by observing the velocity fluctuations on each side of the interface as shown in Figure 4. The left portion of the figure is for the gas whereas the right figure is for the liquid. The gas, as is evident, behaves much like flow over a solid wall. The fluctuations are almost identical to that at a solid boundary, in all directions – streamwise, spanwise, and wall-normal. On the other hand, the liquid, as evident from the figure, has the largest fluctuations in the streamwise and spanwise directions right at the interface itself. It sees the interface virtually as a free slip boundary, except for the mean shear. As a consequence, vertical fluctuations vary as the first power of normal distance, and the square of the normal distance, on the liquid and gas sides, respectively.

These observations are of some importance for the scalar flux on the gas and liquid sides. The mass transfer velocity β^+ is defined as: $\beta^+ = \frac{1}{\sqrt{2ReSc(c_o-c_b)}}\frac{du}{dx_3}$,where $\frac{du}{dx_3}$ is the nondimensional gradient at the interface and c_b and c_o are the bulk and interface concentrations. Mass transfer takes place at the interface by conduction only, therefore it is enhanced when bulk fluid is conveyed to the interface region, e.g. by sweeps. We extend the quadrant analysis and look at the correlation of the Reynolds stress – and therefore of the turbulence structure, in the various quadrants with the instantaneous value of mass transfer velocity β^+ at the interface.

Results are reported in Figure 5 for Sc=1 and Sc=100 on the gas side and liquid sides. In all the cases, except for Sc=100 on the gas side, IV quadrant events (sweeps) are seen to generate the highest values of the mass transfer velocity. This is evident when looking at the probability of such an event to occur (f_p) and at the fraction of the total flux through the interface associated with it (f_h), as in Table I. On the liquid side the sweeps carry a larger fraction of mass flux (~ 0.50), than their probability (~ 0.30). On the liquid side the interface can be efficiently renewed by sweeps, because the horizontal fluctuations are unimpeded. On the gas side the situation in modified by the different boundary conditions. At low Sc number, sweeps and Quadrant I events are seen to be the most efficient for scalar transfer, but when the Sc number increases, and the thermal boundary layer becomes thin, sweeps cannot efficiently penetrate the concentration layer and the role of ejections becomes important as in the Sc=100 case. The vertical velocity fluctuations very close to the interface decrease fast (as $\sim x_3^2$) and limit the mass fluxes.

Table I: Reynold stress and total heat fraction corresponding to II and IV quadrants.

Sc (gas)	1	100	Sc (liq)	1	100
f_p in II	0.36	0.38	f_p in II	0.29	0.32
f_p in IV	0.33	0.32	f_p in IV	0.34	0.37
f_h in II	0.25	0.34	f_h in II	0.15	0.20
f_h in IV	0.46	0.36	f_h in IV	0.52	0.52

In Figure 6 we show a comparison between the DNS results and the prediction of surface renewal theory on the liquid side for Sc=56. Surface renewal theory hypothesizes that the mass fluxes across the interface are enhanced by sweeps of fluid, that bring fresh bulk fluid close to the interface. When a sweep impacts the interface the mass transfer coefficient reaches a maximum and then decaies in time as the near interface fluid saturates, till the region is eventually refreshed by the next sweep.

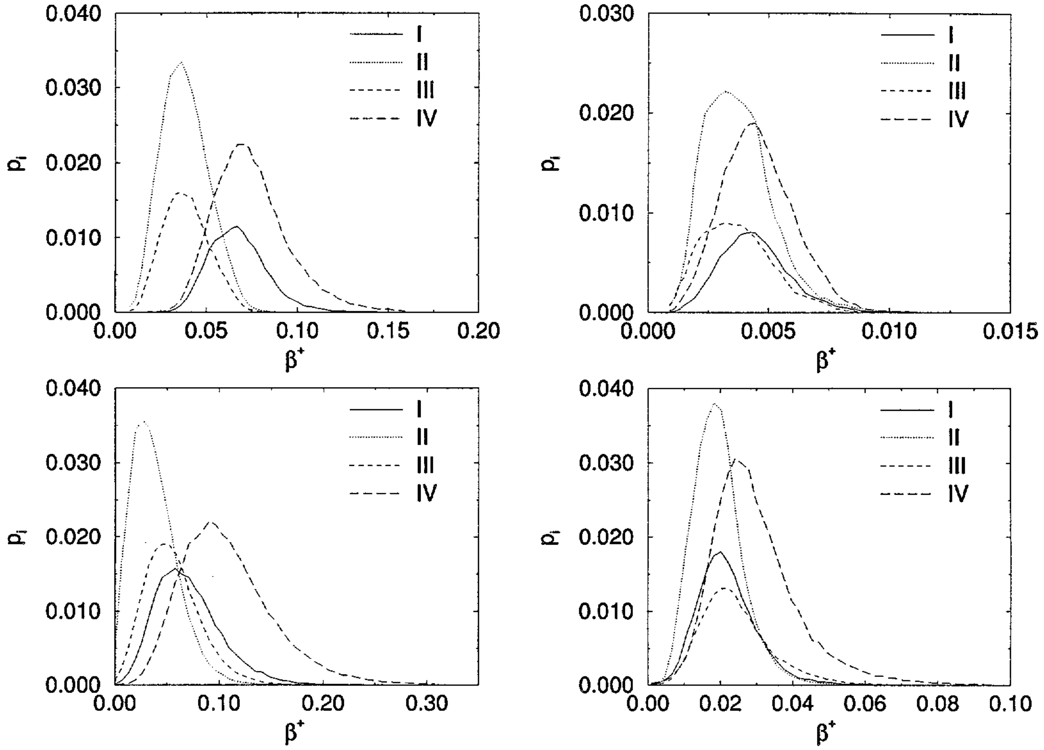

Figure 5: Prob. of strongly coherent events according to quadrant as a function of interfacial flux, β^+, in the region over which the events occur
top: gas; bottom liquid; left Sc=1; right Sc=100

In the bottom of the figure the Reynolds stress and the vertical fluctuating velocity are shown as time proceeds. When they are both negative, a sweep is impacting the interface. In the center figure the corresponding mass transfer velocity is shown and compared to the values predicted by surface renewal theory. The top figure shows the total mass flux over time. The dotted curve in the center and top figures are computed using, respectively, $\sqrt{\frac{D}{\pi t}}$ and $2\sqrt{\frac{Dt}{\pi}}$.

It appears that the mass transfer velocity increases when a sweep is present on the interface. The decay of the mass transfer velocity appears to be faster than $t^{-1/2}$. It should be noticed, however, that the sweep effect persists at the interface and travels with the liquid mean velocity, therefore its effect propagates further along the interface, leaving the point of observation. This means that in a Lagrangian frame, the DNS is closer to the surface renewal theory.

To clarify this point, in Figure 7 we report the contour of the Reynolds stress (bottom) and of the mass transfer velocity (top). The vertical axis is time, and the horizontal the x_1 position. The graph describes how a sweep moves along a line parallel to the streamwise direction, as time passes. The arrows indicate a sweep event and the corresponding mass transfer velocity. The sweep appears to survive for more than 300 wall units, and the patch of high mass flux moves with it.

Based on the results of the quadrant analysis, a model based on surface renewal theory seems appropriate for liquid side mass transfer. Sweeps are seen to control the mass transfer process, and the time history of β^+ in Figure 6 also supports this hypothesis.

On the gas side, at first glance, it seems that this assumption would be less well founded.

In fact we find that all large vertical (interface-normal) velocity fluctuations are responsible for high mass transfer rates. Large vertical fluctuations are, however, mainly related to the bursting process thus also supporting parametrizations based on surface renewal-type models with both sweeps and ejections being important.

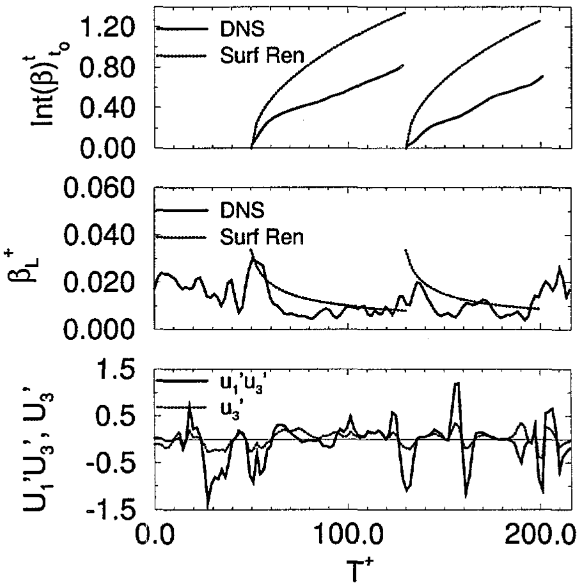

Figure 6: DNS and Surface Renewal theory

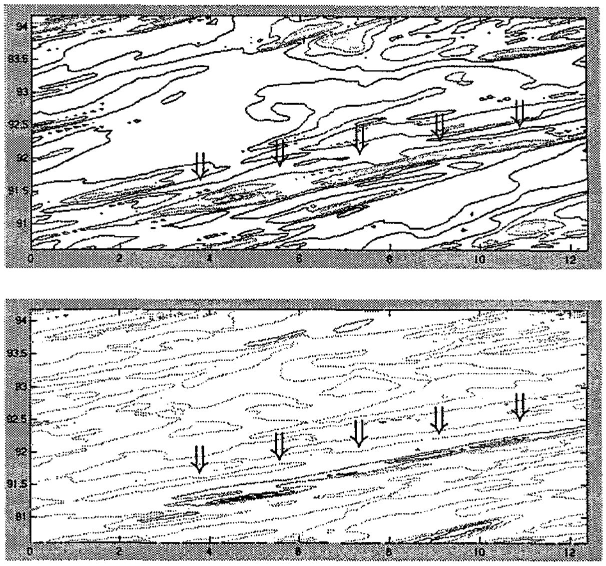

Figure 7: Streaks and β^+ moving at different x_1 locations (horizontal axis), as time progresses (vertical axis)

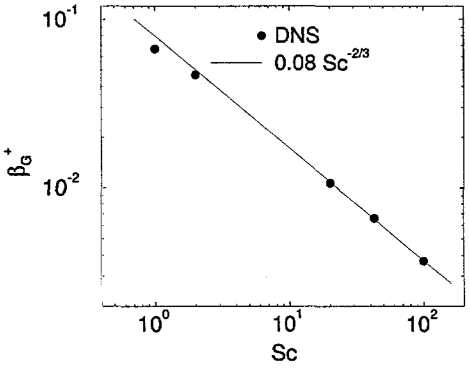

Figure 8.a: β^+ as function of Sc. gas

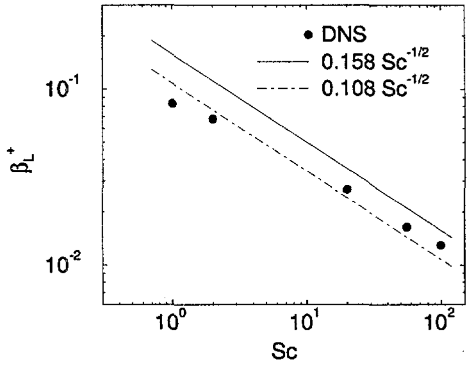

Figure 8.b: β^+ as function of Sc. liq.

The values of β^+ are shown in Figure 8 for the gas and the liquid, and in fact the high Sc number cases are in excellent agreement with correlations proposed by Banerjee [4, 5], based on surface renewal theory. Banerjee assumed that ejections/sweeps (the burst cycle) dominated mass transfer at high Schmidt numbers, and since these events scale with the friction velocity, he was able to derive, for the gas side and the liquid side, respectively, nondimensional mass transfer coefficients as $\beta_g^+ = 0.07$ to $0.09 Sc^{-2/3}$ and $\beta_l^+ = 0.108$ to $0.158 Sc^{-1/2}$.

Support for these correlations comes also from experiments, some of them performed after the correlations where proposed. For the liquid side, the correlation is compared with wind-wave tank data for SF_6 transfer rates from Wanninkhof and Bliven[6] in Figure 9. Again the agreement is good noting that $u_\star$ is probably somewhat over estimated as the form drag was not separated out.

For the gas side the lower bound of the correlation is compared with the moisture transfer data of Ocampo-Torres et al.[7] in Figure 10. The agreement, again, is good.

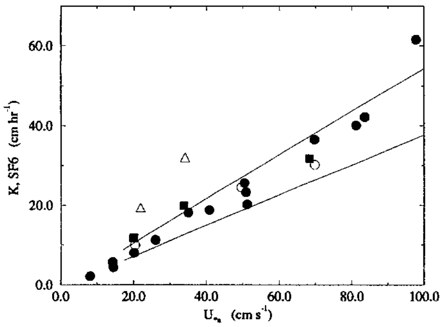

Figure 9: Comparison of $\beta_l^+ = 0.108$ to $0.158 Sc^{-1/2}$ with the data by Wanninkhof and Bliven

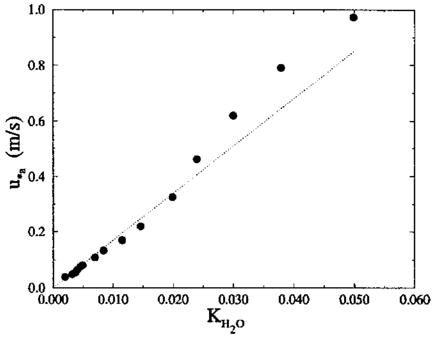

Figure 10: Mass transfer coefficient v.s. $u_\star$ (Ocampo-Torres et al) compared with $\beta_g^+ = 0.07$ to $0.09 Sc^{-2/3}$

3 GAS-LIQUID FLOW NEAR DEFORMING INTERFACES

When the interface is free to deform two new parameters enter into analysis: the Weber number (We) and Froude number (Fr). The cases considered are listed in Table II together with 10 m and 5 m wind velocities.

Table II: Matrix of runs performed.

Case	Fr_τ	We_τ	$u_{\tau g}$	U_5	U_{10}	β_g^+	β_l^+
D1	1.410^{-4}	3.610^{-3}	0.18	4.4	5.5	0.044	0.071
D2	3.910^{-4}	5.010^{-3}	0.26	5.5	7.4	0.041	0.077
D3	5.710^{-4}	5.710^{-3}	0.29	6.0	8.1	0.040	0.075

The wave amplitudes in these cases are less than 2 mm and the wavelength about 4 to 5 cm. The computational domain dimensions are roughly 16 cm in the streamwise direction, 8 cm in the spanwise direction and 2 cm in the interface-normal direction. The domain size is therefore sufficient to capture capillary wave effects.

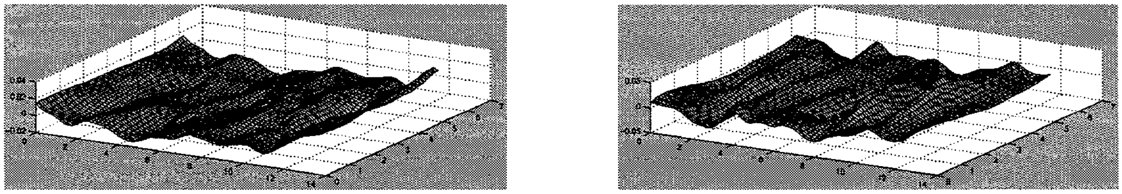

Figure 11: Interface shape, gas on the top, going from left to right, liquid on the bottom, going from right to left. left case D2; right case D3.

In the three cases in Table II, the waves appear to have reached a equilibrium amplitude and steepness. A snapshot of the interface shape is shown in Figure 11, for the D2 and D3 cases. The interface shape becomes more three-dimensional as the wind speed increases, and the amplitude, of course, increases. If the shear stress pattern on the interface is observed, high shear stress regions can be seen over the wave crests, and low shear stress regions over the valleys, as the shear stress pattern is dominated by the gas side. Also the typical streaky structures are similar to those observed in the flat interface case.

Turning now to scalar transfer, we do not observe significant changes in the value of β^+ on the gas and liquid side compared to the flat interface case – for flat interface $\beta_g^+ = 0.043$ and $\beta_l^+ = 0.065$. Changes are of O(5-10%) which is within the statistical error. Having said this, we do observe a slight trend. The value of β^+ on the liquid side is seen first to increase and then to decrease with wave amplitude. On the gas side we observe no significant change. The values are shown in Table II.

The modest increase of β^+ for small wave amplitude on the liquid side has also been observed by Komori et al.[8] in wind-wave tank experiments. Komori at al.[8] observed first a slight increase of β^+ with wave amplitude and then a drop.

5 CONCLUSION

Mass transfer across gas-liquid interfaces has been studied. For flow over a flat interface the effect of the Schmidt number has been investigated. It has been found that large vertical (interface-normal) velocity fluctuations dominate the gas side flux whereas sweeps control the liquid side flux. Both these scale with the friction velocity and support parametrizations presented in this manuscript.

When waves are allowed to form freely on a mobile interface, the value of β^+ is not significantly affected, indicating that the proposed parametrizations are still valid. It appears that such parametrizations also carry over to more complex multiphase flows e.g. bubble columns where Cockx et al.[9] has shown that the proposed correlation holds for the liquid side mass transfer. This is probably because the length scales associated with the sweeps are much smaller than the bubble size and the mean interface structures are similar to those in separated flows.

ACKNOWLEDGEMENT

The work was supported by the U.S. Department of Energy GRANT DE-FG03-85ER-13314.

References

[1] S.J. Kline, W.C. Reynolds, F.A. Schraub, and P.W. Runstadler. The structure of turbulent boundary layers. *J. Fluids Mech.*, 70:741, 1978.

[2] M. Rashidi and S. Banerjee. The effect of boundary conditions and shear rates on streaks formation and breakdown in turbulent channel flow. *Phys. Fluid*, A2:1827, 1990.

[3] P. Lombardi, V. De Angelis, and S. Banerjee. Direct numerical simulation of near-interface turbulence in coupled gas-liquid flow. *Physics of Fluids*, 8(6):1643–65, 1996.

[4] S. Banerjee. A note on turbulent mass transfer at high schmidt numbers. *Chemical Engineering Science*, 26(6):989–90, 1971.

[5] S. Banerjee. Turbulence structure and transport mechanisms at interfaces. *Proceedings of the Ninth International Heat Transfer Conference, Jerusalem, Israel*, pages 395–417, 1990.

[6] R.H. Wanninkhof and L.F. Bliven. Relationship between gas exchange, wind speed, and radar backscatter in a large wind wave tank. *J. of Geophys. Res.*, 96(C2):2785–2796, 1991.

[7] F.J. Ocampo-Torres, F.J. Donelan, J.M. Woollen, and J.R. Koh. Laboratory measurements of mass transfer of carbon dioxide and water vapor for smooth and rough flow conditions. *Tellus Series B*, 46:16, 1994.

[8] S. Komori, R. Nagaosa, and Y. Murakami. Turbulence structure and mass transfer across a sheared air-water interface in wind-driven turbulence. *Journal of Fluid Mechanics*, 249:161–83, 1993.

[9] A. Cockx, M. Roustan, A. Line, and G. Hebrard. Modelling of mass transfer coefficient k_l in bubble columns. *Trans IChemE*, 73-A:627, 1977.

INTERMITTENCY IN MODELS OF TURBULENCE

Robert H. Kraichnan

369 Montezuma 108, Santa Fe, New Mexico 87501

ABSTRACT

The intermittent statistics of the small scales of motion in fully developed Navier-Stokes turbulence remain an outstanding challenge to researchers. Theoretical and computer studies of two simpler systems that share features with Navier-Stokes turbulence, and exhibit intermittency of small scales, are described here. One is Burgers' one-dimensional model of turbulence. The statistics of velocity gradients and velocity differences over small distances are found to exhibit a surprisingly complex structure. The second system is an ensemble of ideal vortices. Analysis of this system implies that the asymptotic scaling exponents for dissipation and squared vorticity in Navier-Stokes turbulence must be equal.

INTRODUCTION

Approximate treatments of the statistics of Navier-Stokes turbulence that proceed systematically from the equations of motion have given good qualitative, and even quantitative, predictions of gross statistical properties like cascade of energy. Higher statistics, particularly those associated with the observed intermittency of small spatial scales are another story. Fractal models of small scales abound, but their connection with the equations of motion is almost nonexistent in most cases. Thus the small scales are an outstanding challenge to theorists. The statistics of small scales are of practical importance, for example in turbulent chemical reactions of non-premixed components.

Burgers' equation describes a one-dimensional infinitely-compressible fluid. It leads to dynamics quite distinct from that of the incompressible Navier-Stokes equation, but both dynamics exhibit cascade of kinetic energy to small scales (large wavenumbers) and the development of intermittency at small scales. In the case of Burgers equation the small-scale intermittency is associated with shock fronts, while in the Navier-Stokes case it is associated with intense vortex structures. Both equations have quadratic nonlinearity. Because of these similarities, Burgers equation has been a testing ground for analytical approaches aimed at the Navier-Stokes equation.

In the past few years a number of papers have attacked the problem of small-scale intermittency in Burgers equation, some invoking current methods of quantum field theory [1-9]. The work to be described here was carried out in collaboration with T. Gotoh [10]. It combines some elementary analysis of ensembles of shocks with exact equations of motion for the probability density function (pdf) of velocity gradient. The predictions were tested by computer simulations. The pdf of gradient is found to have a surprisingly complex structure.

High-Reynolds number Navier-Stokes turbulence exhibits intense worm-like vortices that live in a background of less-structured excitation. These vortices are thought to dominate the higher-order moments of vorticity and the scaling exponents that describe the variation, as powers of r, of moments of the average over regions of size r of vorticity and energy-dissipation. The dissipation associated with an intense cylindrical vortex lies outside the vortex core, and therefore is more spatially diffuse than the squared vorticity. This fact, together with analysis of high-Reynolds-number simulations and experiments has led to the hypothesis that the growth of intermittency of dissipation with decrease of r is asymptotically slower than that of squared vorticity at infinite Reynolds number. That is, the high-order scaling exponents of dissipation are larger than those of squared vorticity.

In work to be summarized here, it is found that this conjectured asymptotic behavior cannot be mediated by cylindrical vortices. The intermittency of dissipation is numerically less than that of squared vorticity at large Reynolds number, but the associated ratios are finite and do not increase indefinitely with Reynolds number. This work was done in collaboration with G. He, S. Chen, R. Zhang, and Y. Zhou

BURGERS TURBULENCE FORCED AT LARGE SCALES

Burgers equation with forcing is

$$u_t + uu_x = \nu u_{xx} + f, \tag{1}$$

where $u(x,t)$ is a one-dimensional velocity field and $f(x,t)$ is a forcing term. The left side of (1) is the Lagrangian time derivative of u, measured along a fluid-element trajectory. Differentiation of (1) yields

$$\xi_t + u\xi_x = -\xi^2 + \nu\xi_{xx} + f_x, \tag{2}$$

where $\xi = u_x$. The ξ^2 term in (2) represents advective gradient intensification or diminution along Lagrangian trajectories. Intensification occurs where $\xi < 0$, leading to the formation of shock fronts. An isolated shock front at large R has the ideal form $\xi(x) \propto -(u_s^2/\nu)\mathrm{sech}^2(u_s x/2\nu)$, where $2u_s$ is the jump in velocity across the shock.

We shall assume that the forcing changes infinitely rapidly in time, and is statistically homogeneous and stationary, with compact spectral support concentrated about a wavenumber k_f. The intensity of forcing of the velocity gradient is measured by

$$B = \int_0^t \langle f_x(x,t) f_x(x,s) \rangle \, ds, \tag{3}$$

where $u(x, t = 0) = 0$ and $\langle\ \rangle$ denotes ensemble average. A characteristic forcing strain rate and Reynolds number induced by the forcing may be defined by $\xi_f = B^{1/3}$ and $R = \xi_f/(\nu k_f^2)$. The steady-state values of rms velocity $u_{rms} = \langle u^2 \rangle^{1/2}$ and typical shock jump induced by the forcing are both $O(\xi_f/k_f)$. The typical shock width is ν/u_{rms} and the typical velocity gradient $\xi = u_x$ at the center of a shock is $R\xi_f$.

An exact equation of motion for the probability distribution function $Q(\xi)$ of ξ follows from (3):

$$\frac{\partial Q}{\partial t} - \frac{\partial}{\partial \xi}(\xi^2 Q) = -\nu \frac{\partial [H(\xi) Q(\xi)]}{\partial \xi} + \xi Q + B \frac{\partial^2 Q}{\partial \xi^2}. \tag{4}$$

Here $H(\xi) \equiv \langle \xi_{xx} | \xi \rangle$ denotes the ensemble mean of ξ_{xx} conditional on fixed ξ. This relation can be derived by following probabilities along Lagrangian trajectories [1,10].

The ξ^2 term in (2) plays two opposed roles. If $\xi < 0$, it intensifies the gradient but, at the same time, squeezes the fluid and thereby decreases the measure along x associated with an interval $d\xi$. If $\xi > 0$, the gradient is decreased but measure is increased by stretching of the fluid. The intensification or diminution of gradient is expressed in (4) by the $\partial(\xi^2 Q)/\partial \xi$ term and the rate of change of measure is expressed by the ξQ term. The B term in (4) expresses in standard fashion the outward diffusion of probability due to infinitely-rapidly-changing forcing.

The ν term in (4) expresses the relaxation of curvature of $u(x)$. It smooths shocks. Regions where $\xi > 0$ are flattened by advection. Thus it is reasonable to assume that the ν term in (4) is negligible if $\xi \gg \xi_f$ and $R \gg 1$. The solution of (4) then has the form

$$Q(\xi) \approx C_+ \xi_f^{-2} \xi \exp(-\xi^3/3B) \quad (\xi \gg \xi_f), \tag{5}$$

where C_+ is a dimensionless constant and the inequality defines the range in which we hope the neglect of viscous effects is justified. The exponential factor in (5) was first found by Polyakov [4], but with a different prefactor. Computer simulations support (5), but a decisive test is difficult because Q falls off so rapidly as ξ increases [10].

The behavior of Q for $R \gg 1$, $\xi < 0$ is more complicated. There is a central peak of width $O(\xi_f)$, followed by a tail for $-\xi \gg \xi_f$. Qualitative analysis of (4) together with analysis of the statistics of an ensemble of idealized sech^2 shocks leads to the following structure for the tail. First there is an intermediate region $\xi_f \ll -\xi \ll R^{1/2}\xi_f$ where $Q(\xi) \propto |\xi|^{-3}$. This represents the transient steepening of regions of negative gradient. Next there is a region $R^{1/2}\xi_f \ll -\xi \ll R\xi_f$ where $Q(\xi) \propto 1/R|\xi|$. This region is supported by the shoulders of mature, long-lived strong shocks. Finally there is a region $-\xi \gg R\xi_f$ where $Q(\xi)$ falls off rapidly (faster than algebraically). This represents the central regions of strong shock fronts. The structure described here is supported by computer simulations in the range $1000 \le R \le 18000$. See Fig. 1.

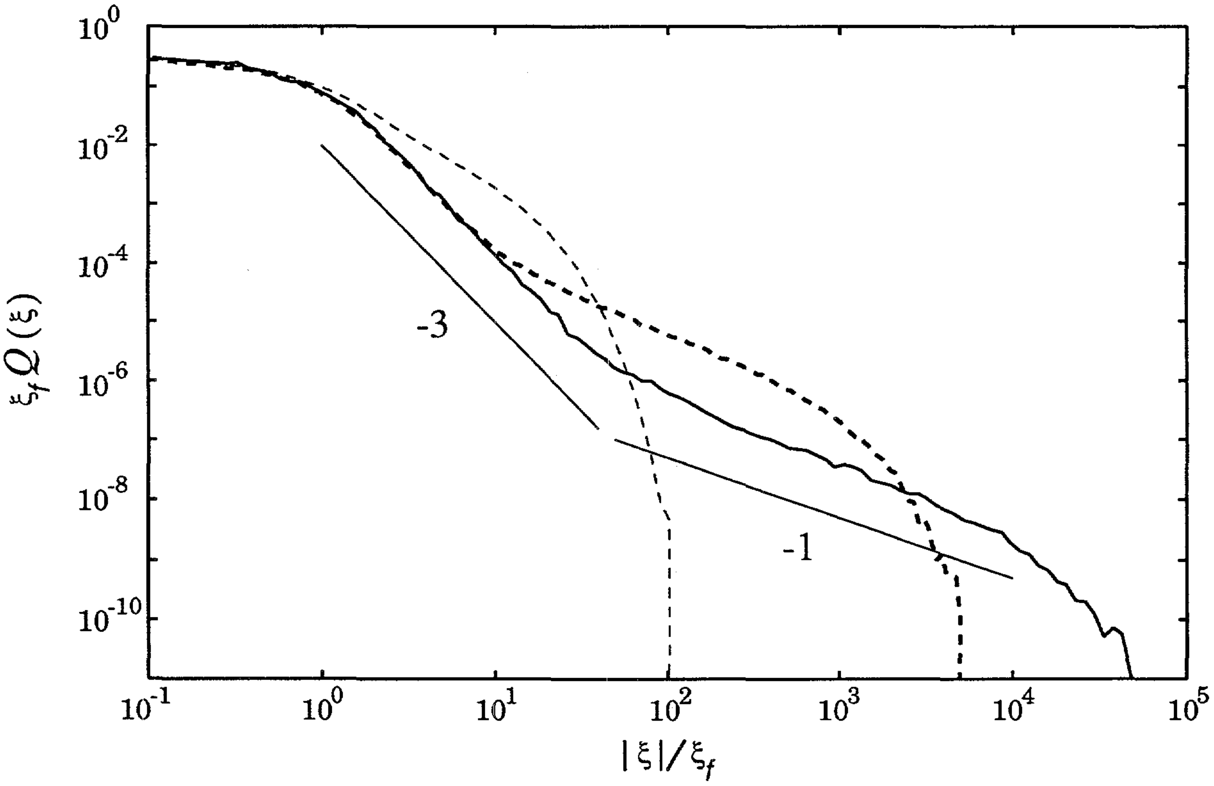

Fig. 1. Logarithmic plot of $\xi_f Q(\xi)$ vs $|\xi|/\xi_f$ for $\xi < 0$ for three steady-state simulations with Reynolds numbers $R = 15$ (light dashed line), $R = 1000$ (heavy dashed line), and $R = 18000$ (solid line).

It is known that that turbulent enstrophy density (squared vorticity magnitude) is more intermittent than the density of dissipation of kinetic-energy. One measure of intermittency of a quantity is the scaling exponents that measure how the ratios of moments of local space averages of the quantity change as the averaging volume decreases. Recent measurements of these exponents computer simulations and experiments suggest that the exponents of enstrophy and dissipation are different [11,12], with the implication that, at infinite Reynolds number, enstrophy is infinitely more intermittent than dissipation.

In recent work, we raise the question of whether any kind of flow structure exists that can support enstrophy that is infinitely more intermittent than dissipation [13]. If such structures do not exist, then the scaling exponents cannot be different as Reynolds number tends to infinity. Our work was confined to cylindrical vortices but we believe the results are generally valid.

In a cylindrical vortex, the only velocity component is the azimuthal component $v_\theta(r)$, where r is distance from the axis. The entrophy density and dissipation density (normalized by viscosity ν) are

$$\Omega(r) = \left(\frac{dv_\theta}{dr} + \frac{v_\theta}{r}\right)^2, \quad \epsilon(r) = \left(\frac{dv_\theta}{dr} - \frac{v_\theta}{r}\right)^2. \tag{6}$$

The enstrophy and normalized dissipation per unit length of vortex are $2\pi \int_0^\infty \Omega(r) r\,dr$ and $2\pi \int_0^\infty \epsilon(r) r\,dr$, respectively. The moments

$$\Omega_n = 2\pi \int_0^\infty [\Omega(r)]^n r\,dr, \quad \epsilon_n = 2\pi \int_0^\infty [\epsilon(r)]^n r\,dr \tag{7}$$

describe the distribution of enstrophy and dissipation densities in the single vortex structure. By (6), $\Omega_1 = \epsilon_1$ if $v_\theta(0) = v_\theta(\infty) = 0$. The sizes of the ratios $R_n = \Omega_n/\epsilon_n$ are measures of how much greater enstrophy intermittency is than dissipation intermittency.

The simplest cylindrical vortex is the Rankin vortex of radius r_0 for which $v_\theta \propto r$ $(r < r_0)$ and $v_\theta \propto 1/r$ $(r > r_0)$. Here the vorticity is confined to a rigidly rotating core and all the dissipation lies outside the core. The ratios R_n calculated from (3) are $R_n = 2n - 1$, corresponding to enstrophy that is modestly more spatially intermittent than dissipation.

We have performed a calculus of variations analysis to find the velocity profile that maximizes R_n. The cylindrical vorticity distribution that maximizes R_2 can be found by solving the associated variational problem, with $\int_0^\infty \omega(r) r\,dr$ and Ω_1 held constant. The result confirms what can be guessed by inspection of (6): The maximizing distribution is the limit $r_1/r_0 \to \infty$ of

$$v_\theta(r) \propto r \quad (r < r_0), \quad v_\theta(r) \propto r^\alpha \quad (r_0 < r < r_1), \quad v_\theta(r) \propto 1/r \quad (r > r_1), \tag{8}$$

with $\alpha = 1/2$. In this case, $R_n = (n-1)9^n$ for $n > 1$. In particular, $R_2 = 81$. Similar profiles, with different values of α maximize R_n for larger n.

The finiteness of these maximal intermittency ratios implies that there is no cylindrical vortex structure that supports asymptotically different scaling exponents for enstrophy and dissipation.

Neither the Rankin vortex nor the vortices with powerlaw cores just described satisfy the Navier-Stokes equation with finite viscosity. An idealized vortex that does satisfy the equation is the Burgers vortex, which is an equilibrium solution in a uniform straining field. For it,

$$v_\theta(r) = \frac{\Gamma}{2\pi}\frac{1-\exp(-r^2/r_b^2)}{r}, \tag{9}$$

where Γ is the total circulation and r_b measures the core diameter. From (6), $\Omega(r) \propto \exp(-2r^2/r_b^2)$, and the vorticity and dissipation overlap. Eq. (6) yields $R_2 \approx 10.65$, $R_3 \approx 104.07$, $R_4 \approx 1040.02$. To a rough approximation, $R_n \sim 10^{n-1}$.

This investigation has demonstrated that any cylindrical vortex gives finite moment ratios R_n of enstropy to dissipation moments. It follows that no ensemble of cylindrical vortices can support different asymptotic scaling exponents for enstrophy and dissipation averaged over a domain of size r. However, large finite values of the R_n are possible. In particular they are achieved by the Burgers vortex, which is a solution of the Navier-Stokes equation. We have found that, as a consequence, ensembles of Burgers vortices can emulate different scaling exponents for enstrophy and dissipation over finite ranges of r [13], in agreement with experimental measurements over finite ranges [12].

CONCLUDING REMARKS

The complexity of statistical structure exhibited by the probability distributions of velocity gradient and velocity differences in Burgers turbulence perhaps is surprising. The question arises of whether this is an indicator that comparable complexity would be found in the statistics of Navier-Stokes turbulence. Some insight may be provided by looking in detail at the statistics of ensembles of ideal vortices, in correspondence to the analysis of ensembles of ideal shocks for Burgers equation. The work on moment ratios associated with ideal Burgers vortices reported here is an elementary step in that direction.

ACKNOWLEDGEMENT

This work was supported by Grant DE-FG03-90ER14118 to Robert H. Kraichnan, Inc. from the U. S. Department of Energy, Office of Basic Energy Sciences, Engineering Research Program.

REFERENCES

[1] T. Gotoh and R. H. Kraichnan, "Statistics of decaying Burgers Turbulence," Phys. Fluids A **5**, 445 (1993); T. Gotoh, "Inertial range statistics of Burgers turbulence," Phys. Fluids **6**, 3985 (1994).

[2] A. Chekhlov and V. Yakhot, "Kolmogorov turbulence in a random-force-driven Burgers equation," Phys. Rev. E, **51**, 2739 (1995); A. Chekhlov and V. Yakhot, "Kolmogorov turbulence in a random-force-driven Burgers equation: anomalous scaling and probability density functions," Phys. Rev. E **52**, 5681 (1995).

[3] M. Avellaneda, R. Ryan, and Weinan E, "PDFs for velocity and velocity gradients in Burgers turbulence," Phys. Fluids **7**, 3067 (1995).

[4] A. M. Polyakov, "Turbulence without pressure," Phys. Rev. E **52**, 6183 (1995).

[5] J.-P. Bouchaud, M. Mézard, and G. Parisi, "Scaling and intermittency in Burgers turbulence," Phys. Rev. E **52**, 3656 (1995); J.-P. Bouchaud and M. Mézard, "Velocity fluctuations in forced Burgers turbulence," Phys. Rev. E **54**, 5116 (1996).

[6] G. Falkovich, I. Kolokolov, V. Lebedev, and A. Migdal, "Instantons and intermittency," Phys. Rev. E **54**, 4896 (1996).

[7] E. Balkovsky, G. Falkovich, I. Kolokolov, and V. Lebedev, "Intermittency of Burgers turbulence," Phys. Rev. Lett. **78**, 1452 (1997).

[8] V. Gurarie and A. Migdal, "Instantons in the Burgers equation," Phys. Rev. E **54**, 4908 (1996).

[9] Weinan E, K. Khanin, A, Mazel, and Y. Sinai, "Probability distribution functions for the random forced Burgers equation," Phys. Rev. Lett. **78**, 1904 (1997).

[10] T. Gotoh and R. H. Kraichnan, "Burgers turbulence with large-scale forcing," submitted to Phys. Fluids (preprint: http://xxx.lanl.gov/archive/chao-dyn/9803037).

[11] S. Chen, K. R. Sreenivasan, M. Nelkin and N. Cao, "A refined similarity hypothesis for tranverse structure functions," Phys. Rev. Lett. **79**, 1253 (1997), S. Chen, K. R. Sreenivasan and M. Nelkin, Phys. Rev. Lett. **79**, 2253 (1997).

[12] K. R. Sreenivasan and R. A. Antonia, "The phenomenology of small-scale turbulence," Annu. Rev. Fluid Mech., **29**, 435 (1997).

[13] G. He, S. Chen, R. H. Kraichnan, R. Zhang, and Y. Zhou, "Statistics of dissipation and enstrophy induced by a set of Burgers vortices," submitted to Phys. Rev. Lett. (preprint: http://xxx.lanl.gov/archive/chao-dyn/9803029).

DYNAMICAL - STATISTICAL MODELING OF TURBULENCE

E. A. Novikov

Institute for Nonlinear Science
University of California, San Diego
La Jolla, CA 92093-0402

ABSTRACT

A general approach to a dynamical-statistical modeling of turbulence is described. The emphasis is on developments in conditional averaging, use of the infinitely divisible distributions, modeling of free-surface turbulence and turbulent boundary layers.

The major goal of turbulence modeling is to slave the enormous number of degrees of freedom in turbulent flows to a selected set of variables, manageable by computer simulations. To do this properly we need to learn a lot about the statistical structure of turbulent flows, which, of course, has independent interest. Different interconnected approaches to turbulence are employed in this work. For example, in the conditional averaging we get as far as we can by manipulating directly with the Navier-Stokes equations (NSE). At the same time, we use general statistical schemes, like Markov processes and infinitely divisible distributions, making them consistent with NSE and with experimental data. We also working on some engineering tools, particularly, for turbulent flows with complex geometry. A general strategy, developed in this work, is summarizes in the Diagram.

The upper horizontal row of four blocks in this Diagram represents various aspects of statistical structure of turbulence and corresponding ingredients of modeling. The first block in this row refers to the Lagrangian and Eulerian description of turbulence in terms of the Markov processes with dependent increments [1-3].

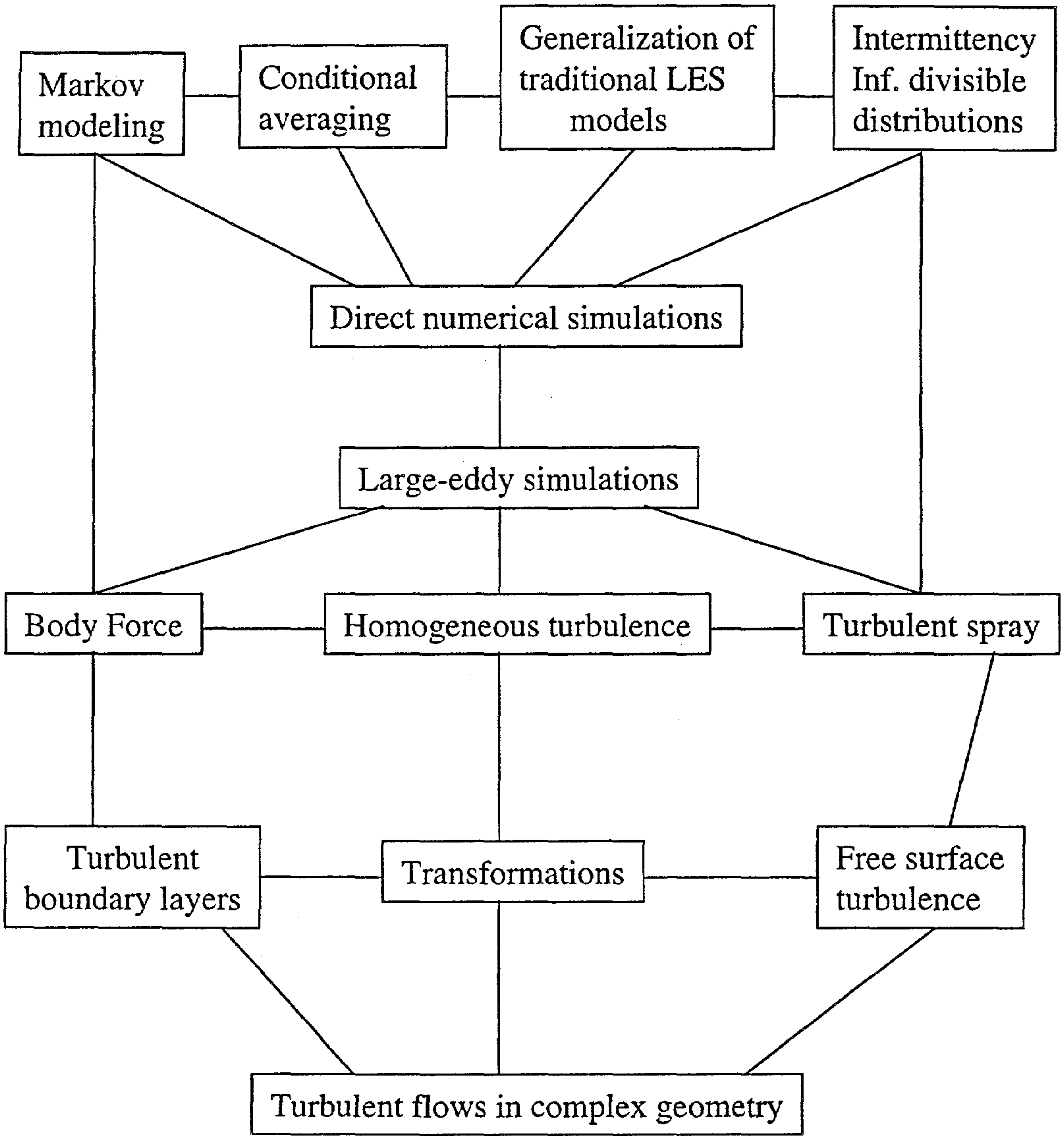

Diagram: Dynamical-statistical modeling of turbulence

This Markov modeling is made statistically consistent with NSE and with experimental data by using the exact relations between the Lagrangian and Eulerian statistics [4].

Markov approach is connected with a body-force technique applicable to turbulent flows in complex geometry (see corresponding blocks in the Diagram). Body force relaxes fluid inside a body and we use the Cartesian grid in numerical simulations instead of the labor-consuming procedures of a mapping of the flow in complex geometry. Such technique is used for a fluid dynamics of the heart [5]. We applied it to a free-surface turbulent flow with a surface piercing body [6].

The second block in the upper row of the Diagram refers to conditional averaging of local characteristics (*lc*) of turbulent flows, which have an internal mechanism of amplification[7]. For three-dimensional (3D) turbulence *lc* is the vorticity field and amplification is due to the vortex stretching [8,9]. For 2D turbulence *lc* is vorticity gradient (*vg*) and amplification is due to compression of fluid particle in the direction of *vg* [10,11]. In both cases the deformation rate tensor, responsible for amplification, is expressed in terms of *lc* and we use the concept of self-amplification. Conditional averaging of NSE written in terms of *lc*, with fixed *lc* in a point, transforms the major nonlinear amplification term into a linear term [10,11]. This allows, particularly, an analytical study of the conditionally-averaged 3D vorticity field:

$$\bar{\Omega}_i(\mathbf{r},\boldsymbol{\omega}) = [f_1(\omega)]^{-1}\int \omega'_i f_2(\mathbf{r},\boldsymbol{\omega},\boldsymbol{\omega}')d\boldsymbol{\omega}' \qquad (1)$$

Here $\mathbf{r}$ is distance from the point with fixed vorticity $\boldsymbol{\omega}$, f_1 and f_2 are the one-point and two-point probability density functions (*pdf*) for the vorticity field. We note that the conditionally-averaged NSE with fixed vorticity in n points corresponds to a hierarchy of equations for the n-point *pdf* [9,11]. For the Fourier-transform of (1) we have general expression [11]:

$$\tilde{\Omega}_i(\mathbf{k},\boldsymbol{\omega}) = g(k,\omega,\mu)(\sigma_i - \mu n_i) + h(k,\omega,\mu)\epsilon_{ijk}\sigma_j n_k \qquad (2)$$

where $\sigma_i = \omega_i\omega^{-1}, n_i = k_i k^{-1}$ are unit vectors of vorticity and of the wavenumber correspondingly, $\mu = \sigma_i n_i$ is their scalar product, ϵ_{ijk} is the unite antisymmetric tensor. In expression (2) we used the local isotropy of turbulence and solenoidality of the vorticity field. Scalar g represents the viscous smoothing of vorticity and it is symmetric function of μ. Scalar h represents vortex stretching and twisting and it is antisymmetric function of μ. For turbulent flows with high Reynolds number $Re = VL\nu^{-1}$(V - characteristic velocity, L - external scale, ν

- kinematic viscosity), it was analytically predicted [10,11] that vortex stretching and twisting is statistically balanced with viscous smoothing on any level of fixed vorticity ω and other terms in the vorticity balance are $\sim Re^{-1/2}$. This prediction was confirmed by direct numerical simulations (DNS) [12,13], which also revealed that the conditionally-averaged rates of vortex stretching and dissipation increase exponentially with ω. This exponential growth of two opposing physical effects can provide a statistical environment for local instabilities and strong fluctuations - formation of strong localized vortices ("vortex strings"), followed by a quick breakdown and twisting of such vortices when they become unstable. Such a picture was observed experimentally [14]. The whole conditionally-averaged vorticity (CAV) field (1) with twisting and hyperboloidal components (2) is obtained from DNS [13]. The characteristic attenuation scale for CAV components is found to be of order ten times bigger than the Kolmogorov microscale $l_\nu = \nu^{3/4} < \varepsilon >^{-1/4}$, where $< \varepsilon >$ is the mean rate of the energy dissipation. The obtained CAV field is in a qualitative agreement with simple analytical model [11]:

$$g(k,\omega,\mu) = \frac{3\nu\omega}{4\pi < \varepsilon >}E(k), \quad h(k,\omega,\mu) = -\frac{15\nu^2 k^2 \mu}{4\pi < \varepsilon >}E(k) \tag{3}$$

where $E(k) = 2\pi < \tilde{\Omega}_i \omega_i >$ is the energy spectrum. However, certain details are different and in future we need a more accurate analytical description of CAV, which can be used in a relaxation subgrid-scale scheme [3,13] for the large-eddy simulations (LES).

It seems natural to choose the grid scale from the hierarchy of increasing scales for coherent structures in 3D turbulence [15,16]:

$$l^{(3)}_{1+m} = LRe^{-3/(10+6m)} \quad (m = 0, 1, 2...) \tag{4}$$

These scales are obtained from a correlation analysis of NSE (with large-scale random forcing) by using a special functional formalism [17,18]. Particularly, at the scale $l_s \equiv l^{(3)}_1 = LRe^{-3/10}$ the nonlinear effects of vortex stretching and convection do not produce flux in the vorticity correlations. Recent experimental data [19] supports the idea [15,16] that scales (4) are relevant to coherent "vortex strings". Analogous hierarchies of scales were obtained also for 2D turbulence from correlation analysis of vg [16] and for passive scalars in 3D and 2D turbulence [20].

Conditional averaging was applied to the free-surface turbulence [21] with use of the fully nonlinear dynamical boundary conditions on free surface. Velocity circulations in free-surface flows were also studied [22].

This leads us to another direction in the conditional averaging, connected with the use of local Lagrangian inviscid invariants of motion. For 3D turbulence we introduced the microcirculations (velocity circulations over infinitesimal fluid contours) [23]. To deal with finite quantities, we let:

$$\gamma^\alpha = \omega_i \sigma_i^\alpha, \quad \sigma_i^\alpha = s_i^\alpha / s_o \tag{5}$$

Here s_i^α is an oriented infinitesimal element of fluid surface, the initial area of surface element s_o is assumed, for simplicity, to be the same for all points and we consider simultaneously three elements $\sigma_i^\alpha (\alpha = 1, 2, 3)$, which are initially orthogonal: $\sigma_i^\alpha \sigma_i^\beta = \delta_{\alpha\beta}$ at $t = 0$. From NSE, written in terms of vorticity:

$$\frac{d\omega_i}{dt} \equiv \frac{\partial \omega_i}{\partial t} + v_i \frac{\partial \omega_i}{\partial x_i} = \frac{\partial v_i}{\partial x_k} \omega_k + \nu \Delta \omega_i, \tag{6}$$

with use of the incompressibility, we get:

$$\frac{d\gamma^\alpha}{dt} = \nu \sigma_i^\alpha \Delta \omega_i, \quad \frac{d\sigma_i^\alpha}{dt} = -\frac{\partial v_k}{\partial x_i} \sigma_k^\alpha \tag{7}$$

These equations, in a sense, separate the effects of viscous smoothing and stretching of vorticity. Based on (7), by using the conditional averaging (with fixed vorticity), a statistical evolution of microcirculations and fluid surface elements are studied (particularly, initial tendencies) with various initial orientations of fluid contours relative to the vorticity field [23].

For 2D turbulence, we introduced the Lagrangian infinitesimal increments of vorticity [24]:

$$\sigma^\alpha = s_i \rho_i^\alpha, \quad s_i = \frac{\partial \omega}{\partial x_i}, \quad \rho_i^\alpha = r_i^\alpha / r_o \tag{8}$$

Here r_i^α $(\alpha = 1, 2)$ are linear infinitesimal fluid elements with initial length r_o (the same for all points) and initially orthogonal: $\rho_i^\alpha \rho_i^\beta = \delta_{\alpha\beta}$. From NSE, written in terms of vg:

$$\frac{ds_i}{dt} = -\frac{\partial v_k}{\partial x_i} s_k + \nu \Delta s_i, \tag{9}$$

using the incompressibility, we get:

$$\frac{d\sigma^\alpha}{dt} = \nu \rho_i^\alpha \Delta s_i, \quad \frac{d\rho_i^\alpha}{dt} = \frac{\partial v_i}{\partial x_k} \rho_k^\alpha \tag{10}$$

These equations separate the effects of linear diffusion and nonlinear sharpening of vg. From (10), by using conditional averaging (with fixed vg), we studied statistical evolution of vorticity increments and fluid elements with various mutual orientations[24]. We also used the fact, established in our numerical experiments [25]:

$$\beta(s) = \overline{\frac{\partial v_i}{\partial x_k}} \frac{s_i s_k}{s^2} < 0 \tag{11}$$

Here overbar means conditional averaging with fixed vg, $\beta(s)$ is the conditionally averaged deformation rate with fixed s_i. The physical meaning of inequality (11) is that the effect of nonlinear sharpening of vg in 2D turbulence statistically persists on all levels of s.

The third block in the upper row in the Diagram refers to traditional subgrid-scale (SGS) models (Smagorinsky [26], Bardina [27]) and their broad generalizations [28,29]. These models, generally, can serve some engineering goals. However, they may insufficiently reflect the physics of turbulence. Particularly, the widely used Smagorinsky model, by design, reproduce the "5/3" energy spectrum ($E(k) \sim < \varepsilon >^{2/3} k^{-5/3}$), but our numerical experiments show that this model gives incorrect third order moment (flux of energy) and incorrect high order moments (intermittency).

This leads us to the last block in the upper row. The effects of intermittency are described in terms of the breakdown coefficients (*bdc*) for the energy dissipation [30]. These *bdc* are shown to be an alternative to the multifractal formalism [1]. An intermittency correction was obtained for a simple SGS model [1]. The phenomena of scale similarity and intermittency were imbedded into the theory of the infinitely divisible distributions [31]. This allows us to use the well developed mathematical apparatus [32]. The results are compared with experimental data corresponding to $Re \sim 10^7$[33]. The *bdc* approach and the theory of infinitely divisible distributions were recently applied to the phenomena of turbulent spray [34] (see corresponding block in the Diagram) and can be readily applied to turbulent bubble flows. Turbulent spray and bubble flows are important in many areas of engineering.

Related to this is our work on more general problems of the free-surface turbulence [29,35]. Here, along with high resolution DNS, we use some transformations from homogeneous to nonhomogeneous turbulence [36] and a level set approach [6], which significantly simplifies numerical simulations. For free-surface turbulent flows with surface piercing bodies, as a starting point, we used the following transformation:

$$v_i = \frac{\partial b_i}{\partial x_k} w_k - b_k \frac{\partial w_i}{\partial x_k} + (c - \frac{\partial b_k}{\partial x_k}) w_i \tag{12}$$

Here v_i is the velocity fluctuation in a nonhomogeneous turbulent flow with the mean velocity profile u_i ; velocity w_i , produced by LES, is solenoidal ($\frac{\partial w_k}{\partial x_k} = 0$) and statistically homogeneous in horizontal plane (with a nonlinear free-surface approach or a low Frude-number approximation); constant c we can put equal to zero for a turbulent wake; b_i is a deformation of the flow and, in first approximation, we used $b_i = \tau u_i$, where τ is a characteristic time of the flow. The velocity field (12) is solenoidal and if we choose τ constant, then deformation is also solenoidal and the last term in (12) is zero (with $c = 0$). Transformation (12) is suggested by the Poisson-bracket form of the nonlinear terms in NSE. Comparison of this transformation with experimental data [36] shows, that the correlation coefficient, calculated in terms of turbulent energy $\frac{1}{2} < v_i^2 >$, is surprisingly high (≥ 0.8). Transformation (12), which is designed for a distant part of the wake, can be generalized, for example, by using several successive transformations in order to get closer to a body.

Another development is in the modeling of turbulent boundary layers (TBL). Such modeling is important by itself and also is very useful for a boundary condition in LES. A variational approach to TBL is developed [37]. Particularly, for a turbulent flow along a cylinder with radius a, we get the following equation for the mean velocity profile $u(r)$:

$$\pi \frac{\delta}{\delta u} \int (\frac{du}{dr})^2 r dr = \lambda (\frac{du}{dr})^2 \tag{13}$$

Here $\delta/\delta u$ stands for the variational (functional) derivative, λ is the eigenvalue of this variational operator applied to the enstrophy of the mean flow. A unique solution of this equation, which recovers the standard logarithmic profile (for the flat boundary) on distances $z \equiv r - a \ll a$, has the form:

$$u = \frac{u_*}{\kappa} \{ \ln[a_+ \ln(z_+/a_+ + 1)] + b \} \tag{14}$$

Here u_* is the friction velocity, $\kappa \approx 0.4$ is the Karman constant, $a_+ = a/z_*$, $z_* = \nu/u_*$ is the thickness of the viscous sublayer, $z_+ = z/z_*$ and $b \approx 2$ is the empirical constant in the standard logarithmic profile, corresponding to a hydrodynamically smooth boundary. The variational eigenvalue $\lambda = \kappa/u_*$ is, thus, determined by the momentum flux, which is equal to u_*^2. Experimental data fits well [37] into the double-logarithmic profile (14).

Various aspects of turbulence, represented by blocks in the Diagram, are fruitful areas of research. By putting them together, we reveal the important connections, leading to more general methods of turbulence modeling.

ACKNOWLEDGMENT

This work is supported by the U. S. Department of Energy.

REFERENCES

1. E. A. NOVIKOV, *Phys. Fluids* **A1**, 326 (1989); *Phys. Fluids* **A2**, 814 (1990); *Phys.Rev.* **A46**(10), R6147 (1992).

2. G. PEDRIZZETTI and E. A. NOVIKOV, *J. Fluid Mech.* **280**, 69 (1994).

3. E. A. NOVIKOV, "Conditionally-averaged dynamics of turbulence, new scaling and stochastic modeling", in "*Lévy Flights and Related Topics in Physics*" (eds. M. Shlesinger, G. Zaslavsky and U. Frish), pp 35-50, Springer, 1995.

4. E. A. NOVIKOV, *Appl. Math. Mech.* **33**, 862 (1969); *Phys. Fluids* **29**, 3907 (1986).

5. C. S. PESKIN, *Bull. Amer. Phys. Soc.* **42** (11), 2207 (1997).

6. D. G. DOMMERMUTH, E. A. SCHLAGETER, J. C. TALCOTT, D. C. WYATT and E. A. NOVIKOV, *Bull. Amer. Phys. Soc.* **42** (11), 2196 (1997), also preprint.

7. E. A. NOVIKOV, *Fluid Dyn. Res.* **6**, 79 (1990).

8. G. I. TAYLOR, *Proc. Roy. Soc. London* **A164**, 15 (1938).

9. E. A. NOVIKOV, *Dokl. Akad. Nauk SSSR* **12**, 299, (1967) [*Sov. Phys. Dokl.* **12**, 1006 (1968)].

10. E. A. NOVIKOV, "Solution of exact kinetic equations for intermittent turbulence", Proc. of Monte-Verita Sympos. (1991), *New Approaches and Concepts in Turbulence* (edited by T. Dracos and A. Tsinober), Birkauser, Basel, pp.131-139, 1993; *Phys. Lett.* **A162**, 385 (1992); *J. Phys.* **A25**, L657 (1992); "Exact results obtained by conditional averaging of Navier-Stokes equations", in *Turbulence in Spatially Extended Systems* (eds. R. Benzi, C. Basdevant and S. Chiliberti), pp. 101-106, Nova Scince Publishers, 1993.

11. E. A. NOVIKOV, *Fluid Dyn. Res.* **12**, 107 (1993).

12. E. A. NOVIKOV and D. G. DOMMERMUTH, *Modern Phys.Lett.* **B8**

(23), 1395 (1994).

13. R. C. Y. MUI, D. G. DOMMERMUTH and E. A. NOVIKOV, *Phys. Rev.* **E53** (3), 2355 (1996).

14. S. DOUADY, Y. COUDER and M. E. BRACHET, *Phys. Rev. Lett.* **67**, 983 (1991), and video produced by these authors.

15. E. A. NOVIKOV, *Phys. Rev. Lett.* **71**(17), 2718 (1993).

16. E. A. NOVIKOV, *Phys. Rev.* **E49**(2), R975 (1994).

17. E. A. NOVIKOV, *Zh. Eksp. Teor. Phys.* **47**, 1919 (1964) [*Sov. Phys. JETP* **20**, 1290 (1965)].

18. W. D. McCOMB, *The Physics of Fluid turbulence,* Claredon, Oxford, 1990, p. 554 (Appendix H).

19. P. TABELING, private communication (1998).

20. E. A. NOVIKOV, *J. Phys. A, Math. Gen.*, **27** L797 (1994).

21. E. A. NOVIKOV, *Phys. Rev.* **E52**, 5679 (1995).

22. E. A. NOVIKOV, *Int. J. Eng. Sci.* **34**, 359 (1995).

23. E. A. NOVIKOV, *Phys. Rev.* **E52**(3), 2574 (1995).

24. E. A. NOVIKOV, *Phys. Lett.* **A236**, 65 (1997).

25. A. E. NOVIKOV and E. A. NOVIKOV, in preparation.

26. J. SMAGORINSKY, *Mon. Weather Rev.* **91**, 99 (1963).

27. J. BARDINA, J. H. FERZIGER and W. C. REYNOLDS, AIAA 80-1357 (1980).

28. T. S. LUND and E. A. NOVIKOV, *Ann. Res.,* Stanford, 27 (1992).

29. D. G. DOMMERMUTH and E. A. NOVIKOV, "Direct-numerical and large-eddy simulations of turbulent free-surface flows", Proc. Sixth Internat. Conf. on Numerical Ship Hydrodynamics, Iowa City, pp.239-270 (1993).

30. E. A. NOVIKOV, *Appl. Math. Mech.* **35**, 231 (1971).

31. E. A. NOVIKOV, *Phys. Rev.* **E50**(5), R3303 (1994).

32. W. FELLER, *An Introduction to Probability Theory and its Applications,* V.2, Wiley, 1991, reprint from 1966-edition.

33. G. PEDRIZZETTI, E. A. NOVIKOV and A. A. PRASKOVSKY, *Phys. Rev.* **E53**(1), 475 (1996).

34. E. A. NOVIKOV and D. G. DOMMERMUTH, *Phys. Rev.* **E56**(5), 5479 (1997).

35. D. G. DOMMERMUTH, E. A. NOVIKOV and R. C. Y. MUI, "The interaction of surface waves with turbulence", Proc. of ASMA Symp. on Free-Surface Turbulence, Lake Tahoe, 20 pages, 1994.

36.D. G. DOMMERMUTH, M. GHARIB, H. T. HUANG, G. I. INNIS, P. MAHEO, E. A. NOVIKOV, J. C. TALCOTT and D. C. WAYATT, "Turbulent free-surface flows: a comparison between numerical simulations and experimental measurements", Proc. 21-st Symp. on Naval Hydrodynamics, Trondheim, Norway, 17 pages, 1996.

37. E. A. NOVIKOV and D. G. DOMMERMUTH, "A variational approach to turbulent boundary layers", in *Fundamental Problematic Issues in Turbulence* (eds. A. Gyr, P. Monkiewitz and A. Tsinober), Birkauser, Basel, 1998, to be published.